Aerospace Science and Technology 108 (2021) 106364

Contents lists available at ScienceDirect

Aerospace Science and Technology

www.elsevier.com/locate/aescte

Flow structure of pressure transmission tube and its influence on unsteady pressure measuring results in compressible flow

Xiaotong Tong [a,b], Qifan Zhang [a,*], Lianjie Yue [a,b], Xinyu Zhang [a,b]

[a] State Key Laboratory of High-temperature Gas Dynamics, Institute of Mechanics, Chinese Academy of Sciences, Beijing 100190, China
[b] School of Engineering Science, University of Chinese Academy of Sciences, Beijing 100049, China

ARTICLE INFO

Article history:
Received 31 December 2019
Received in revised form 11 November 2020
Accepted 12 November 2020
Available online 23 November 2020
Communicated by Kostas Kontis

Keywords:
Unsteady pressure measurement
Pressure sensor
Pressure transmission tube
Dynamic response
Compressible flow

ABSTRACT

The computational fluid dynamics method is introduced to study the dynamic response of pressure transmission tubes in compressible flow. A simple theoretical model based on the flow structure was developed to reveal the physical mechanism of the tube dynamic response. According to the dominant variables in the model, the influence of Mach number, tube configuration and tube cooling was numerically studied with CFD tools. The CFD results indicate that the dynamic response characteristics of a given tube in compressible flow are significantly different from that in incompressible flow, which is important to the improvement of measurement accuracy in supersonic aerodynamic experiments. The tube effect in compressible flow includes the tap-flow interaction at the entrance of the tube and the signal damping inside the tube, and the latter is less important. The tap-flow interaction makes the pressure at the pressure tap different from the true wall pressure, and as a result the traditional models are inappropriate in compressible flow. The constraint of mass flow rate caused by the tap-flow interaction contributes mainly to the pressure signal distortion in compressible flow, which was not considered in existing incompressible flow studies. The measuring pressure amplitude mainly depends on the mass flow rate through the pressure sensing hole and the stagnation enthalpy change of the inflow gas in the charge process. The influence of tube configuration is negligible for incompressible flow and low-frequency input signal, but significant for compressible flow and high-frequency signal. Generally, the measuring pressure amplitude of straight tubes is closer to the true value than that of mixed diameter tubes. It is discovered that the cooled tube wall causes more serious pressure signal damping than the adiabatic tube wall. Tube cooling can reduce the amplitude ratio by 0.1 in high enthalpy flow. In addition, a method of rapid estimation of amplitude ratios is developed based on the CFD database.

1. Introduction

Measurement of wall static pressure with pressure transducers fixed to the test model surface is a basic technology in most aerodynamic experiments. Because of the complexity of test models, the size of pressure transducers, the high temperature of gases and the lash against pressure transducers in high speed airflow, it is difficult to make the pressure transducer chip flush with the test model surface. Therefore, pressure measurement systems (Fig. 1) with the pressure sensing hole, the pressure transmission tube and the pressure transducer connected are commonly used to measure wall static pressure. This method is widely used in steady pressure measurement. However, the gas in the pressure transmission tube always acts as a signal filter when the system measures unsteady pressure [1]. As a result, the transducer cannot sense the pressure change near the pressure sensing hole timely and the measuring results are distorted compared with the true pressure signals. The pressure transmission tube usually causes much larger measurement uncertainty than the pressure sensor component.

Since 1960s, much research has been conducted and a lot of theoretical models have been developed to estimate the pressure signal changes caused by pressure transmission tubes and to correct the measuring results ([2] reviews existing models). Several new models have been developed in recent years. Hall and Povey [2] highlighted the fluidic behavior and wave propagation in the tube and proposed a new simplified model. Antonini et al. [3] established a dynamic response model of complex pressure transmission tubes system based on mass conservation and viscous and thermal frequency-dependent effects. Whitmore and Fox [4] derived a second-order model directly from the infinite-order Bergh and Tijdeman solution [5]. Kutin and Svete [6] supplemented Berg and Tijdeman model with thermodynamic effects and extend this

* Corresponding author.
E-mail address: zhangqifan@imech.ac.cn (Q. Zhang).

https://doi.org/10.1016/j.ast.2020.106364
1270-9638/

Nomenclature

A_b	Bleed hole Area	m^2
Δm	in/out flow mass	kg
Δp	Amplitude of unsteady pressure	kPa
c	Speed of sound	$m\,s^{-1}$
c_p	Specific heat capacity	$J\,kg^{-1}\,K^{-1}$
d_1	Diameter of the thin tube	mm
d_2	Diameter of the thick tube	mm
f	Pressure fluctuating frequency	Hz
h	Specific enthalpy	$J\,kg^{-1}$
H	Enthalpy	J
l_1	Length of the thin tube	mm
l_2	Length of the thick tube	mm
m	Mass of the gas	kg
Ma	Oncoming Mach number	
N	Number of infinitesimal time segments	
p	Mean pressure	kPa
$p(t)$	Unsteady pressure	kPa
p_{plen}	Suction backpressure in ref. [47]	kPa
p_t	Oncoming stagnation pressure in ref. [47]	kPa
q_m^*	Sonic mass flow rate	$kg\,s^{-1}$
$q_m(t)$	Mass flow rate	$kg\,s^{-1}$
q_{heat}	Heat flux	$J\,s^{-1}$
R	Gas constant	$J\,kg^{-1}\,K^{-1}$
T	Pressure fluctuating Time period	s
t	Time	s
t_0	Start time of charge	s
T_1	Oncoming static temperature	K
T_0	Stagnation temperature	K
V	Volume of tube	m^3
W_{sonic}	Sonic mass flow coefficient	
x	X-coordinate	mm
y	Y-coordinate	mm
z	Z-coordinate	mm

Greeks

α	Stagnation temperature ratio
γ	Ratio of specific heats
δ	Thickness of boundary layer (mm)
η	Equilibrium stagnation temperature ratio
θ	Phase shift (degree)

Subscripts

0	Stagnation value
1	True or ideal value, value outside tube
2	Measuring value, value inside tube
h	Value at the pressure sensing hole
i	Sequence number for summation
in	Upstream input pressure signal
max	Maximum value, wave crest
mean	Mean value
min	Minimum value, wave trough
outside	Value outside the tube
steady	Value in the initial steady flow field
t	Inflection point of q_{2max}
u	Upper limit of q_{2max}

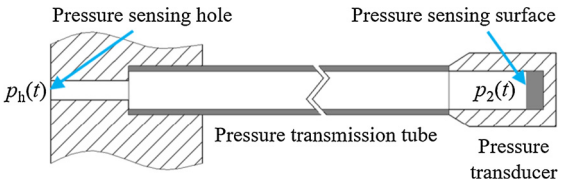

Fig. 1. Measurement system with pressure sensing hole, pressure tube and transducer.

model to liquid-filled pressure measurement systems. Most existing models, nevertheless, depend on many variables and are too complicated for practical application. Only professional researchers skilled in theoretical modeling and mathematics can deal with more than twenty equations and the parameters of the same number correctly in different situations, which may be the reason why these models are not widely used in aerospace engineering. Additionally, the exact flow structures inside/outside the tube are not considered or described in detail by all the existing models.

To validate theoretical models [2–5] or apply the inverse correction method [7], experimental methods for the calibration of tube dynamic response have been developed [8–12]. In most calibration experiments, a sine-like periodic pressure signal is imposed as the input signal, and it is measured by two pressure transducers at the same time. One transducer is close to the signal source while the other transducer and the signal source are linked by a pressure transmission tube. The dynamic response characteristic (i.e. transfer functions) of the pressure transmission tube is determined by comparing the measuring results of these two transducers. Semaan and Scholz [12] experimentally calibrated the dynamic response of tubes and compared the effects of different Fourier transform schemes for inverse correction. Kim et al. [13] applied pressure transfer function determined by experiments to airfoil pressure measurement. The transfer function based on Bergh-Tijdeman solution was also used in NASA transonic wind tunnel [14]. Kozmar and Laschka [15] investigated the effect of the pressure tap cavity in a wind tunnel with a maximum flow velocity of 60 $m\,s^{-1}$. Nikoueeyan et al. [16] compared the measuring results of different tube configurations in subsonic wind tunnel experiments. Gejji et al. [17] developed a dynamic calibration device based on a gas turbine combustor and compared dynamic characteristics of different transducer installations. Fotia et al. [18] experimentally studied the response of tubes to non-linear pressure fluctuations with a rotating detonation engine. Sahin and Schiffmann [19] used a siren disk to reproduce periodic flows for dynamic calibration and introduced a modified correction method based on Fourier series. These calibration experiments were mostly conducted in static air or subsonic airflow, but the calibration results in incompressible flow may be invalid for compressible flow because of the strong interaction between the pressure tap and the cross flow.

The tap-flow interaction in steady pressure measurement was studied in low-speed airflow [20–23]. There is a similar problem named probe-flow interaction [24,25] in static pressure probes [26–28]. Giulia Dell'Era et al. [24,25] pointed out that the probe-flow interaction was an important error source in unsteady pressure measurement. Bouhanguel et al. [29,30] studied the flow structure and the steady pressure measuring results of the pressure probe in supersonic ejectors by computational fluid mechanics (CFD) tools and experiments. The results indicated that the presence of the probe caused significant disturbances. However, the unsteady tap-flow or probe-flow interaction in high-speed airflow has not been studied systematically.

In recent years, flush-mount microelectromechanical systems (MEMS) sensors [31] without pressure tubes have been developed, and the "true" pressure on the wall can be measured directly. Nevertheless, the flush-mount sensor is vulnerable in high-temperature gas. For example, Naples et al. [32] used a flush-

mount sensor in a rotating detonation engine, but the sensor burned off within a few seconds. The conditions in supersonic or hypersonic experiments (e.g. scramjet) are usually harsher because of the drastic airflow lash, aerodynamic heating and combustion heat release. Though high-temperature piezoelectric [33], piezoresistive [34–36] and fiber optic [37] sensors at 600–1000 °C have been developed, flush-mount sensors are not robust and affordable enough in the turbojet [38] and scramjet combustor [39,40] with a 1300–2000 °C static temperature. Therefore, water cooled pressure sensors with tubes [41,42] and pressure probes [38,43] are still used in high enthalpy airflow. With the increasing high-speed aerodynamic tests including the supersonic inlet [44,45], isolator [46] and combustor [39,40,47,48] of the scramjet, the influence of pressure transmission tubes on unsteady pressure measuring results in supersonic flow needs studying. The effect of tube cooling should also be assessed.

The dynamic response of pressure transmission tubes is essentially a flow phenomenon governed by Navier-Stokes (N-S) equations, and various theoretical models are simplifications of N-S equations on different assumptions. CFD technology for solving N-S equations has progressed remarkably nowadays and has been used in flow rate measurement, such as pressure probes [29], pneumatic components [49], Venturi nozzles [50,51], stacks [52] and fuel gear flowmeters [53]. The tap-flow interaction in unsteady pressure measurement can also be simulated by CFD tools and the response of the measurement system can be predicted easily. On the other hand, it is quite difficult to impose an ideal controllable sine pressure signal to a supersonic flow field and the influence of pressure transmission tube in supersonic flow is hard to study with experiments. Hence a novel CFD method is introduced to study the tube response in this work. Sine pressure signals are added to the flow field, and the influence of oncoming Mach number, tube configuration and tube cooling on tube dynamic response are obtained with CFD tools. The physical mechanism of tube dynamic response is studied with a new simple model and the CFD results.

2. Numerical method and validation

2.1. Physical model

The pressure measurement problem in a pipe was chosen to be numerically simulated. The physical model consisted of a rectangular section pipe and a pressure transmission tube connected to the upper wall of the pipe, as shown in Fig. 2. The sizes of the rectangular section pipe in the x, y and z direction were 70 mm, 50 mm and 50 mm respectively to make sure the cubage of the main flow-path was greatly larger than the pressure transmission tube. Because mixed diameter tubes were commonly used in practice to make sure the spatial resolution of pressure measurement, the tube consisted of two sections - the thin tube directly connected to the pipe wall and the thick tube connected to the pressure transducer. The diameters and lengths of the two sections were d_1, d_2 and l_1, l_2, respectively. The types A–C in Table 1 were used in practice to match the 2 mm diameter transducer volume. Note that type D and E were straight tubes ($d_1 = d_2$). As a contrast, the no-tube type G was included to obtain true wall pressure.

2.2. Numerical method

The commercial CFD software FLUENT was used to conduct three-dimensional unsteady numerical simulations. The compressible perfect gas N-S equations were discretized by finite volume method. The pressure-based solver and the pressure-velocity coupled algorithm were employed because the flow inside/outside the pressure transmission tube were incompressible/compressible respectively. In addition, specific heat was calculated by the polynomial about temperature, and viscosity was solved by Sutherland's formula. The Spalart-Allmaras turbulence model [54], which is suitable for wall-restrained flow and shear layer flow was used to close the equations. The discretization of pressure, density, momentum, modified turbulent viscosity and energy were of second order and the transient formulation was set as second order implicit.

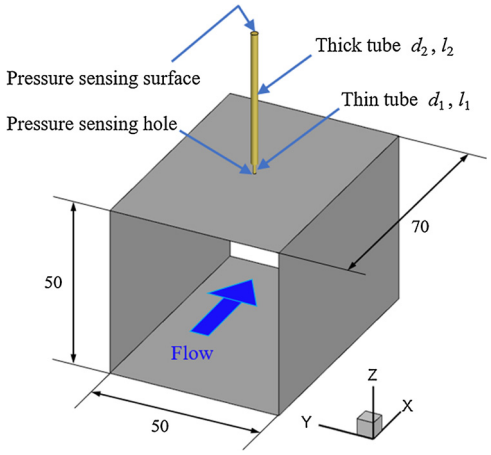

Fig. 2. Schematic of rectangular section pipe with a pressure transmission tube (unit: mm).

Table 1
Configurations of the pneumatic tubes.

Type	d_1/mm	l_1/mm	d_2/mm	l_2/mm	V/mm^3
A	0.8	3	2	20	64.34
B	0.8	3	2	40	127.2
C	0.8	3	2	80	252.8
D	0.8	43	-	-	20.11
E	1.94	43	-	-	127.2
F	0.8	3	1.4	40	63.08
G	-	-	-	-	0

The computational grid and boundary conditions are shown in Fig. 3. The solution domain was discretized by structured grid and the grid were densified in the near-wall region to ensure the y^+ accorded with requirements of S-A model (The recommend y^+ range for S-A model is $y^+ < 1$ or $y^+ > 30$). The grid of type B contained about 950 000 cells. In calculation, the adiabatic walls were imposed on all the solid wall except for the tube cooling cases in section 4.4, and the static pressures at the center of pressure sensing hole and the center of pressure sensing surface (top wall of the tube) were monitored.

The Mach number, boundary layer thickness and static pressure at the entrance of the rectangular pipe were given by the User-Defined Function (UDF) provided by FLUENT. The boundary layer thickness is 2 mm and velocity profile in the boundary layer was given according to the 1/7 power law. The sine pressure signal given by the UDF can be written as

$$p_{\text{in}}(t) = p + \Delta p \sin(2\pi f t) \tag{1}$$

in which $p_{\text{in}}(t)$ is the entrance pressure as a function of time t, and p, Δp and f are mean pressure, amplitude of pressure fluctuating and the fluctuating frequency respectively. For all the cases in this paper, p was 202.6 kPa and Δp was 101.3 kPa.

The static temperature of incoming flow, T_1, was 300 K, and the Mach number of the main flow ranges 0.2–4.0. For all the cases, the time step size was 1/1000 of a pressure fluctuating period to achieve high time resolution (e.g. the time step size for a 500 Hz signal is 1/500/1000 s $= 2 \times 10^{-6}$ s, and the sampling rate is 500 kHz) and enough inner iteration steps were conducted

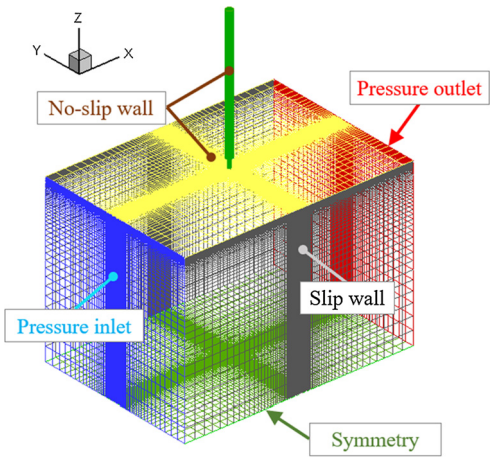

Fig. 3. Grid and boundary conditions.

Table 2
Grid convergence for *Ma*2.5 flow.

Grid No.	Δz_{min}/mm	Cells/1000	y^+	$q_{max}/(10^{-5}$ kg s$^{-1})$
1	0.05	780	33	8.02
2	0.05	2550	33	8.31
3	0.01	850	6.0	8.10
4	0.01	2550	6.0	7.85
5	2×10^{-3}	950	1.2	8.12
6	2×10^{-3}	2550	1.2	8.11
7	1×10^{-3}	1520	0.7	8.11

to make sure the residuals declined at least three orders of magnitude in a time step. The convergency of the transient calculation is verified in Appendix A. Each case was calculated until the mean pressure, the amplitude and the fluctuating period at the pressure sensing surface stabilized and at least three continual periods were obtained.

2.3. Grid convergence

Seven computational grids for type *B* were tested to determine the grid sensitivity. The grid parameters are shown in Table 2, in which the Δz_{min} is the minimum cell height near the pressure sensing hole and the y^+ is the minimum wall y^+ near the pressure sensing hole. Grid 3, 5 and 7 were only refined in the near wall region compared with grid 1. Grid 2, 4 and 6 were refined in the entire solution domain. The maximum mass flow rates through the pressure sensing hole for different grids are also compared in Table 2, in which the q_{max} for grid 5–7 agrees well. Fig. 4 presents the time-varying pressure at the center of the pressure sensing surface under No. 4 flow condition ($Ma = 2.5$, $p = 2$ atm, $\Delta p = 1$ atm) at the frequency of 500 Hz. The pressure-time curves of grid 5–7 coincide in Fig. 4, which indicates that $p_2(t)$ is independent of the cells number for these grids. Therefore, grid 5 was selected to ensure calculation accuracy and save computing resource.

2.4. Numerical method validation for incompressible flow

Numerical simulations were conducted for incompressible dynamic response cases and the CFD result was compared with the experimental results in [5]. The solution domain is shown in Fig. 5. The diameter and length of the tube were 1.0 mm and 500 mm respectively. The static temperature for the pressure outlet was 297 K. Sine pressure signals ($p = 102970$ Pa, $\Delta p = 637.43$ Pa) were imposed at the entrance of the tube and the pressure at the pressure sensing surface was monitored. Cases with frequencies of 25–200 Hz were calculated and the pressure signals for f

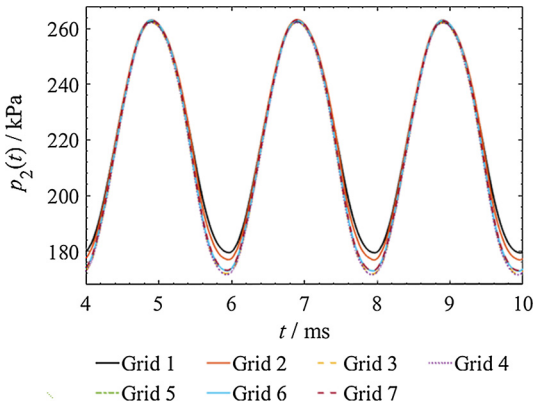

Fig. 4. Pressure-time curves of the central point of the pressure sensing surface for different grids.

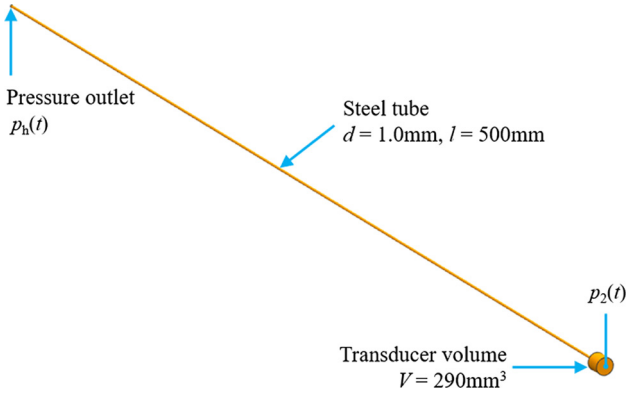

Fig. 5. Solution domain of incompressible validation cases.

$= 160$ Hz is shown in Fig. 6(a), in which $p_2(t)$ is a smooth sine signal. Fig. 6(b) shows the amplitude ratios and Fig. 6(c) shows the phase shifts between $p_h(t)$ and $p_2(t)$. The CFD result agrees well with the experimental data and the maximum error of $\Delta p_2/\Delta p_1$ is about 5%. Thus, the numerical method is accurate and suitable for incompressible tube response cases.

2.5. Numerical method validation for compressible flow

The dynamic calibration experiment in supersonic flow is difficult and has not been reported. Hence the steady supersonic boundary layer bleed experiment with similar configurations and flow structure can be used to validate the CFD method. If the bleed mass flow rate at different pressure ratios can be calculated accurately with the CFD tools, it is reasonable to believe that the relation between the mass flow rate and the inner/outer pressure can also be calculated accurately for pressure transmission tube cases. The results of the bleed experiments [55] at NASA Glenn Research Center were chosen for validation. Fig. 7 shows the physical model for the validation cases. At 49.2 mm upstream the bleed hole, the Mach number of the main flow is 1.33, the stagnation pressure p_t is 275.8 kPa, the Reynolds number is 2.46×10^7, the boundary layer thickness is 13.2 mm, and the stagnation temperature T_t is nominally ambient (300 K) according to experimental results [55]. These parameters were imposed at the entrance of the rectangular pipe with UDF in calculations.

Steady numerical simulations were conducted according to the test model configuration and flow conditions in [55] with the numerical method introduced above. For different bleed plenum pressures, the mass flow rates and the sonic flow coefficient W_{sonic} were obtained. The sonic flow coefficient is an important param-

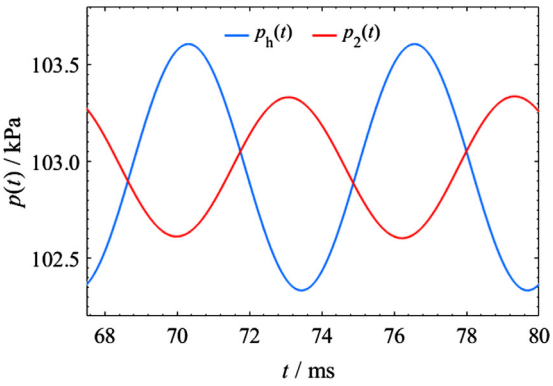

(a) Pressure signals for f=160Hz.

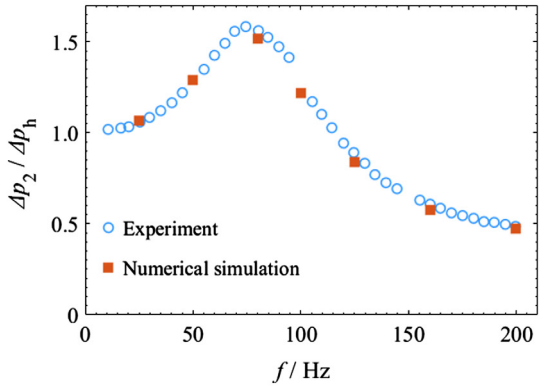

(b) Amplitude ratios for different frequencies.

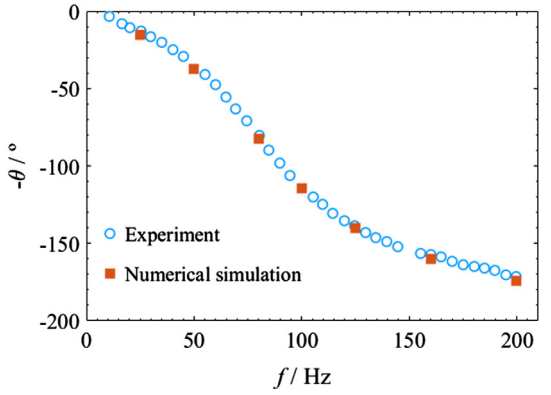

(c) Phase shifts for different frequencies.

Fig. 6. Calculated pressure signals and comparison of the transfer functions between CFD and experiment.

eter for boundary layer bleed [55,56] and is generally used to validate CFD methods [56–59]. W_{sonic} is defined as:

$$W_{\text{sonic}} = \frac{q_m}{q_m^*} \tag{2}$$

where q_m is the mass flow rate through the hole, and q_m^* is the mass-flow rate under choked conditions:

$$q_m^* = p_t A_b \sqrt{\frac{\gamma}{RT_t}} \left(\frac{2}{\gamma+1}\right)^{\frac{\gamma+1}{2(\gamma-1)}} \tag{3}$$

For the given flow conditions, q_m^* is 18.27 $\times$ 10^{-3} kg s^{-1}.

A typical x-z slice of the flow field near the bleed hole is shown in Fig. 8(a). There are shock wave and shear flow in the bleed hole in Fig. 8(a) and this flow structure also exists in pressure sensing holes, which makes it difficult to predict the unsteady pressure

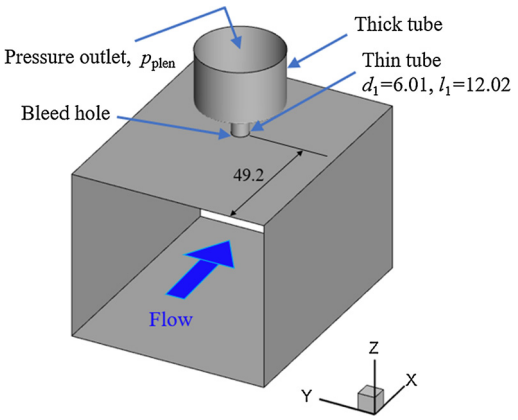

Fig. 7. Tunnel walls and bleed hole for compressible validation case (unit: mm).

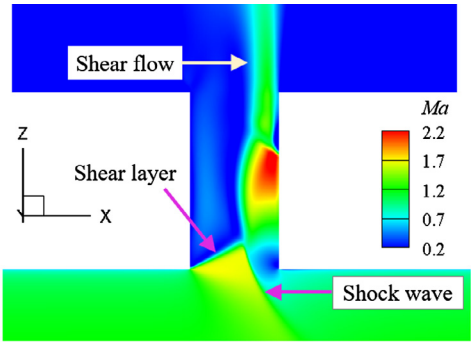

(a) Ma contour at p_{plen}/p_t=0.169

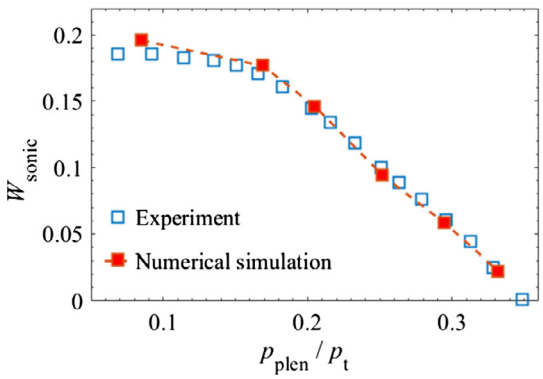

(b) Sonic flow coefficient W_{sonic} as a function of p_{plen}/p_t

Fig. 8. Calculated Mach contour and comparison of the sonic flow coefficients between CFD and experiment. (For interpretation of the colors in the figure(s), the reader is referred to the web version of this article.)

at the entrance of the tube and the mass flow rate analytically with existing models. As shown in Fig. 8(b), W_{sonic} as a function of normalized bleed plenum pressure p_{plen}/p_t obtained by experiments and numerical simulations agree well. The maximum error of W_{sonic} is about 5%, and the numerical and experimental results agree better for larger p_{plen}/p_t. Thus, the CFD method is suitable for compressible small hole flow.

Because the CFD results of incompressible and compressible cases agree well with experimental results, the numerical method is valid and appropriate for the pressure transmission tube cases.

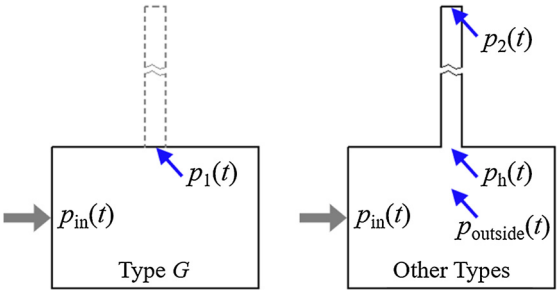

Fig. 9. Positions of monitor points (no tube for type G).

3. Flow structure and theoretical analysis

The interaction between the gas flowing into/out of the pressure transmission tube and the main flow outside the tube is significant when the main flow is supersonic. This is the main difference between high-speed cases and low-speed cases. Thus, it is necessary to analyze the flow structure of the pressure tube in compressible flow. Then the dominant physical variables can be identified and a simple theoretical model can be obtained to explain basic physical mechanism in the dynamic response of tubes.

3.1. Tap-flow interaction at the entrance of the tube

In incompressible flow, the pressure signal is transmitted from the main flow to the pressure tap, and then the inner tube. Hence the flow structure at the entrance of the tube was first analyzed. Numerical simulations of type B and G ($Ma2.5$, $f = 500$ Hz) were conducted to reveal the tap-flow interaction in compressible airflow. It is found that the pressure at the pressure sensing surface distributed uniformly, so the pressure at the central point of the pressure sensing surface can be used to characterize the pressure signals received by the transducer. To avoid confusion, the true wall pressure (calculated on type G) was named $p_1(t)$, and the pressure at the pressure sensing hole was named $p_h(t)$, and the pressure at the pressure sensing surface (measuring results calculated on type A–F) was named $p_2(t)$, as shown in Fig. 9.

The pressure signals of different positions are compared in Fig. 10. The figure illustrates that $p_1(t)$ differs from $p_{in}(t)$ a bit for the different streamwise positions of the pressure monitor points. $p_h(t)$ significantly deviates from $p_1(t)$, but $p_2(t)$ slightly deviates from $p_h(t)$, i.e. the signal damping in the tube is less significant than the signal distortion at the entrance of the tube. The amplitude and mean of the pressure signals are compared in Table 3, in which the amplitude of $p_2(t)$ is less than $p_1(t)$ and the mean of $p_2(t)$ is slightly greater than $p_1(t)$. Additionally, $p_{outside}(t)$ (the pressure signal at 10 mm vertically outside away from the pressure sensing hole) is almost the same as $p_1(t)$, which indicates that the tube effect in compressible flow can be divided into two parts: the tap-flow interaction near the entrance of the tube and the signal damping in the tube, and the former is dominant.

The Mach number and streamline distribution in the middle x-z section of the pipe are displayed in Fig. 11. During the charge (Fig. 11(a)) and discharge (Fig. 11(b)) process of the tube, there is a significant velocity difference between the inside-tube region and the main flow out of the tube. The flow structure in Fig. 11(a) is similar to that of the bleed hole in [55,56,59]. The compressible shear layer [60–62] interacts with the trailing edge of the pressure tap, which causes a shock wave and the shear flow in the tube. In Fig. 11(b), a transverse jet, weaker than the most studied cases [63–65], interacts with the cross flow. As a result, a small separation region appears and acts as a aerodynamic wedge which obstructs the upstream boundary layer flow (similar flow structure was studied in [66–68]).

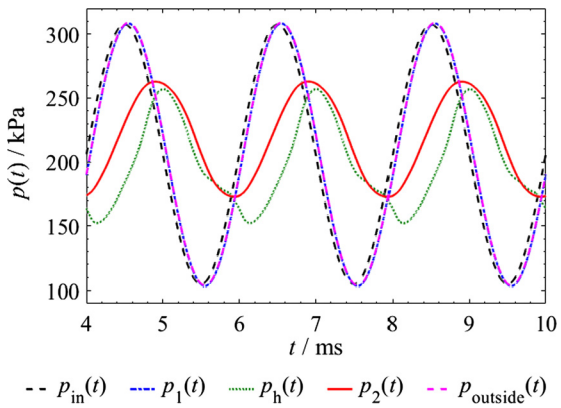

Fig. 10. Pressure-time curves for different monitor points (500 Hz, type B and G).

Table 3
Amplitudes and means of pressure-time curves (type B and G).

Curve	Amplitude/kPa	Mean/kPa
$p_{in}(t)$	101.3	202.6
$p_1(t)$	101.3	202.6
$p_h(t)$	65.83	199.1
$p_2(t)$	44.93	217.8
$p_{outside}(t)$	101.3	202.6

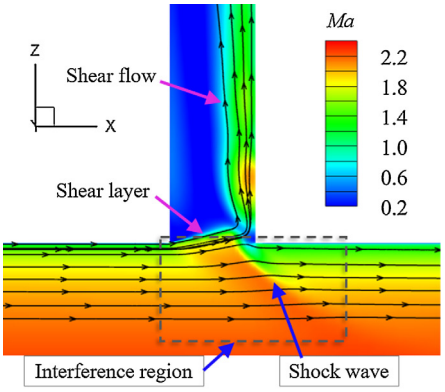

(a) charging (when inflow $q_m(t)$ reaches the maximum)

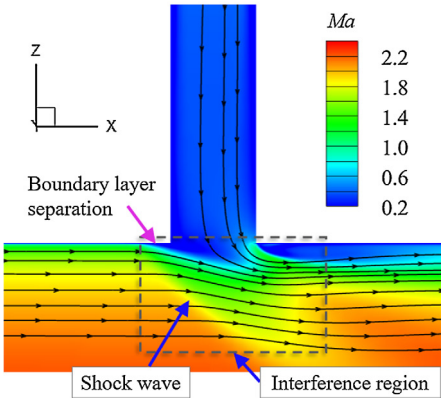

(b) discharging (when outflow $q_m(t)$ reaches the maximum)

Fig. 11. Mach number and streamline distribution (500 Hz, type B, x-z section).

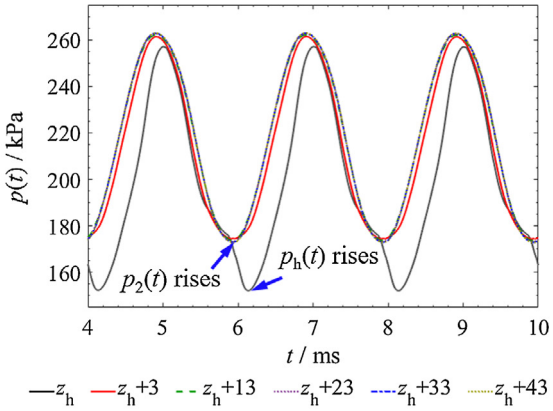

(a) Pressure signals at different positions in the tube (z_h corresponds to the tube entrance).

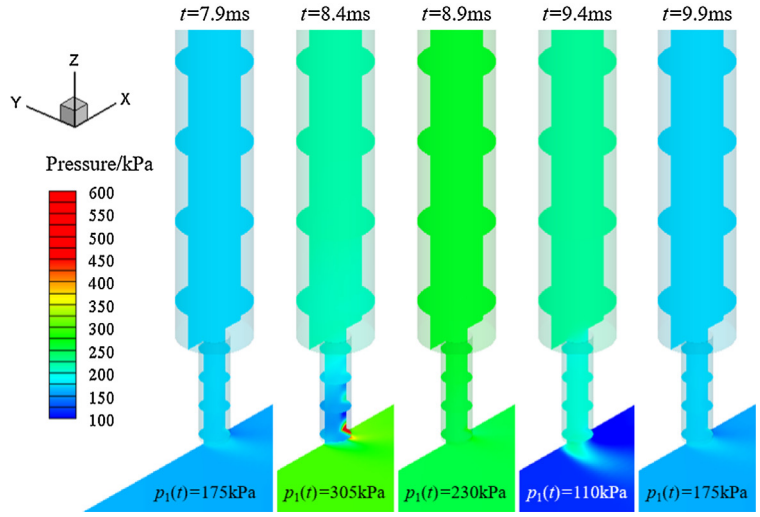

(b) Pressure distribution at typical times.

Fig. 12. Pressure distribution characteristics in the tube ($f = 500$ Hz).

The gas flowing into/out of the tube interacts with the main flow, and this phenomenon, named as tap-flow interaction, includes two aspects. Firstly, the main flow limits the mass flow rate through the pressure sensing hole. The streamlines passing through the tube converge at the trailing edge of the pressure sensing hole and the effective flow area at the pressure sensing hole narrows (see Fig. 11). Secondly, the tube influences the main flow and makes the streamlines under the pressure sensing hole deflect. The feature scale of the interference region (grey square frames in Fig. 11) where streamlines deflect 1–2 times the diameter of the pressure sensing hole. As a result of these two factors, $p_h(t)$ differs from $p_1(t)$ significantly.

In low-speed airflow, $p_h(t)$ closely approximates $p_1(t)$ because the tap-flow interaction is weak. Existing research regarded $p_h(t)$ as reference pressure signal [2,5,6] and obtained the relation between $p_h(t)$ and $p_2(t)$ by modeling or experiments. But the true wall pressure $p_1(t)$ and the relation between $p_1(t)$ and $p_2(t)$ are more important in practical measurement, and as analyzed above, $p_h(t)$ is markedly different from $p_2(t)$ in high-speed airflow. This means that $p_h(t)$ cannot be predicted by existing theoretical models, and it is not an appropriate reference pressure signal in high speed airflow. In this paper, the true wall pressure $p_1(t)$ is regarded as reference pressure signal and the relation between $p_1(t)$ and $p_2(t)$ is mainly studied.

3.2. Flow structure in the tube

For incompressible flow, the flow for each streamwise section in the tube is uniform. However, there is supersonic shear flow inside the tube according to Fig. 11(a), which influences the tube response. Hence the flow structure in the tube B is analyzed in Figs. 12–14.

The pressure signals at six positions along the axis of the tube are shown in Fig. 12(a), in which $z_h = 50$ mm corresponds to the pressure sensing hole. The pressure signals at $z = 53$ mm–93 mm are almost the same, whereas the pressure signals at $z = z_h$ is different from the signals at other positions. Most signal distortion happens in the thin part of the tube rather than in the thick part, which indicates that the signal damping in the thick tube is negligible. Therefore, the difference between $p_1(t)$ and $p_2(t)$ is mainly caused by the pressure tap-cross flow interaction and the internal flow structure near the entrance of the tube.

Fig. 12(b) further shows the pressure distribution at typical times in a period. The $p_2(t)$ rises during $t = 7.9$–8.9 ms and drops during $t = 8.9$–9.9 ms. At $t = 8.4$ ms, there is a high-pressure region at the entrance of the tube because the shear layer impacts on the tube wall. The pressure distribution on the entrance cross section is inhomogeneous, which is different from that in incompressible flow. In the charge process, the pressure in the thick tube is higher than that in the thin tube as a result of the shear flow

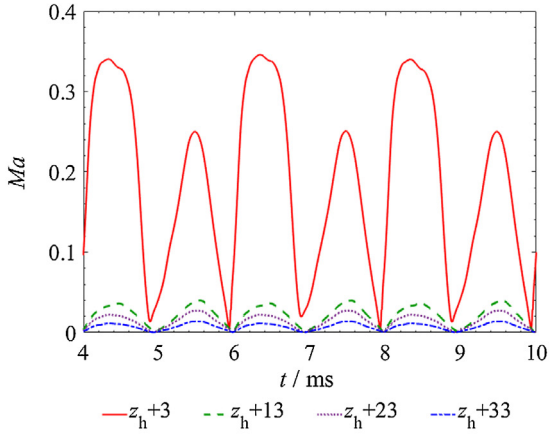

(a) *Ma* at different positions in the tube.

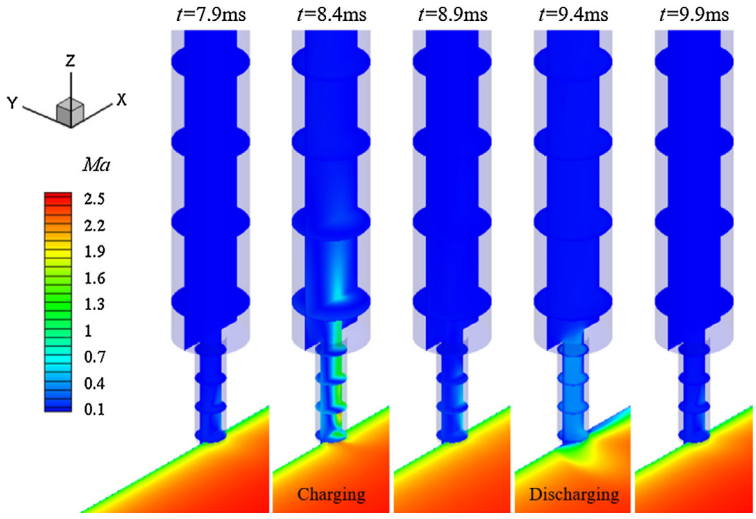

(b) *Ma* distribution at typical times.

Fig. 13. Mach number distribution characteristics in the tube ($f = 500$ Hz).

in the thin tube. This is the reason why $p_h(t)$ ($z = z_h$) lags behind $p_2(t)$ ($z = z_h + 43$) in the charge process in Fig. 12(a).

In Fig. 13(a), the Mach number at $z = z_h + 3$ varies with time and shows two crests at $t = 8.4$ and 9.4 ms, whereas the Mach number in the thick tube remains lower than 0.04. Fig. 13(b) shows that there is supersonic shear flow in the thin tube at $t =$ 8.4 ms. The supersonic flow in the tube is faster than the pressure waves, hence the $p_2(t)$ rises earlier than $p_h(t)$. On the contrary, the flow in the thin tube at $t = 9.4$ ms is subsonic and relatively homogeneous. Fig. 14(a) indicates that the temperature in the tube fluctuates around 560 K, which is close to the inner temperature in the initial steady flow field. The maximum temperature difference in the tube is about 20 K, which is negligible because the region with higher temperature is only a small part of the tube. The temperature shows the same trends over time as the $p_2(t)$. In Fig. 14(b), the temperature in the tube is homogeneous when the $p_2(t)$ reaches the p_{2max} or p_{2min}, and the flow field in the tube approximately reaches thermal equilibrium.

Figs. 12–14 indicate that the gas properties (pressure and temperature) are homogeneous when the $p_2(t)$ reaches the p_{2max} or p_{2min}. Therefore, the axial inhomogeneity of the flow structure can be ignored and the theoretical analysis can be simplified. Note that the flow structure is also related with the sudden expansion configuration of the tube, which may affect the measuring results (see section 4.2).

3.3. Theoretical analysis

The mass and heat transfer characteristics of the tube in the charge and discharge process are influenced by the flow structure. If the mass and heat transfer is analyzed with existing modeling methods, it is necessary to introduce many variables and equations. Hence a simple model is proposed based on the flow structure to explain the physical mechanism of tube dynamic response. Because short tubes are generally used to achieve high resonance frequency of the measurement system in high-speed aerodynamic experiments, the following sections focus on short tubes.

Suppose pressure waves propagate inside the tube with the sonic speed c, the reciprocating motion of a pressure wave within the common range of frequency spends a time of $2L/c$. For short tubes, this time is much less than a period of the unsteady pressure signal outside the tube (the time of pressure waves propagation can be ignored), i.e. $2L/c \ll 1/f$. As a result, the pressure distribution in the tube is uniform at a certain time and can be characterized by $p_2(t)$, which is also illustrated in Fig. 12(a).

With dynamic equilibrium of the flow field inside/outside the tube established, the fluctuating period of $p_2(t)$ is the same as that of $p_1(t)$. Fig. 15 illustrates that when $p_2(t) < p_1(t)$, the outer gas flows into the tube (i.e. the mass flow rate $q_m(t) > 0$) and the pressure in the tube rises. When $p_2(t) > p_1(t)$, the inner gas flows out of the tube (i.e. $q_m(t) < 0$) and the pressure in the tube drops. Consider the charge process in Fig. 15, which begins at $t = t_0$,

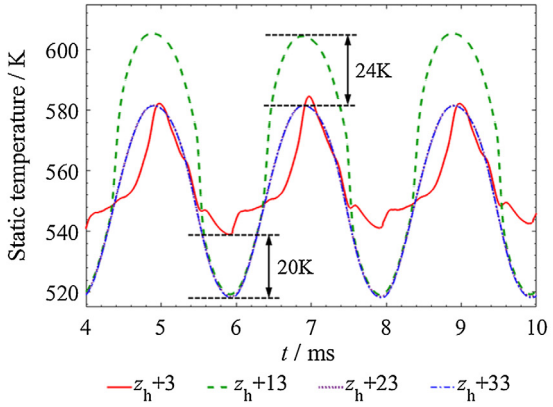

(a) Static temperature at different positions in the tube.

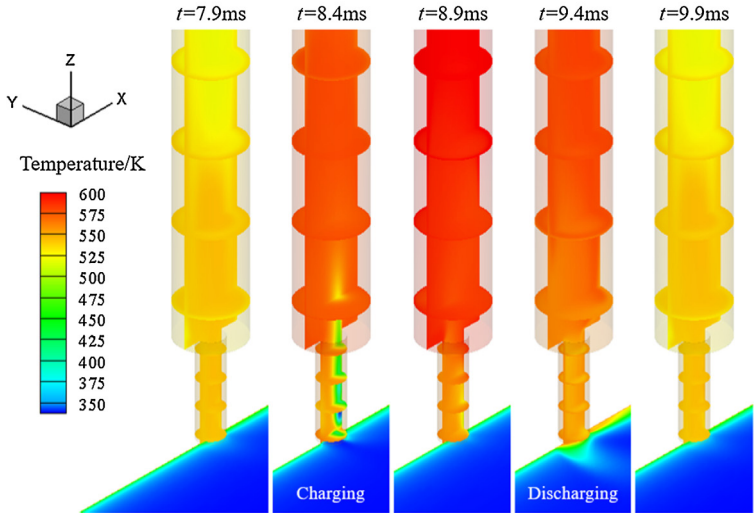

(b) Static temperature distribution at typical times.

Fig. 14. Static temperature distribution characteristics in the tube ($f = 500$ Hz).

$p_2(t_0) = p_{2\min}$ and ends at $t = t_0 + T/2$, $p_2(t_0 + T/2) = p_{2\max}$. In fact, the charge process lasts for a time slightly less than $T/2$ because of the supersonic shear flow in the thin tube. Here this time is denoted by $T/2$ for simplicity and the accurate time is used in CFD data processing (see section 4). Gas flows into the tube through the pressure sensing hole continuously during the charge process, accordingly, the mass flow rate $q_m(t) > 0$ and the total inflow mass is denoted by $2\Delta m_2$. Note that the inflow mass during a charge process is equal to the outflow mass during a discharge process because of the periodicity of the flow.

Except the mass balance, the energy transfer during the charge/discharge process is also important to reveal the tube dynamic response mechanism. Considering the gas temperature change during the charge/discharge process is less than 200 K and the specific heat changes little within this temperature range, assumption of calorically perfect gas is introduced to describe the energy transfer briefly. Thus, the static enthalpy per mass for the main flow is:

$$h_1 = c_p T_1 = \frac{\gamma}{\gamma - 1} R \tag{4}$$

where c_p is specific heat capacity and R is gas constant. The stagnation enthalpy, which characterizes the total energy of the gas, includes static enthalpy and dynamic energy. The stagnation enthalpy is defined:

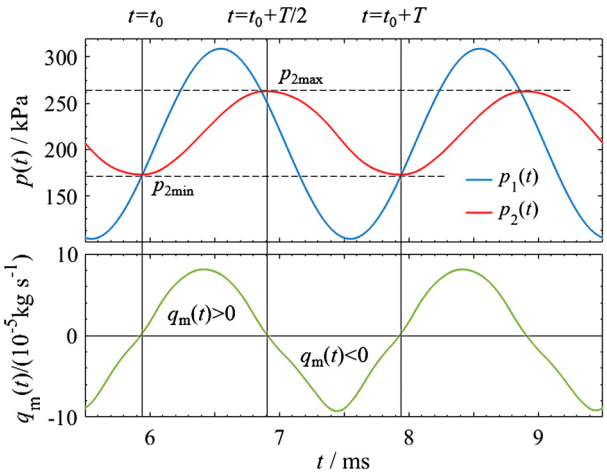

Fig. 15. Correspondence between $p_2(t)$ and $q_m(t)$ in a fluctuating period ($f = 500$ Hz).

$$h_{01} = c_p T_1 + \frac{1}{2} U_1^2 = c_p T_{01} \tag{5}$$

in which U_1 is flow velocity and T_{01} is stagnation temperature:

$$U_1^2 = Ma_1^2 \gamma R T_1 \tag{6}$$

$$T_{01} = T_1 + \frac{U_1^2}{2c_p} = T_1 \left(1 + \frac{\gamma - 1}{2} Ma_1^2\right) \tag{7}$$

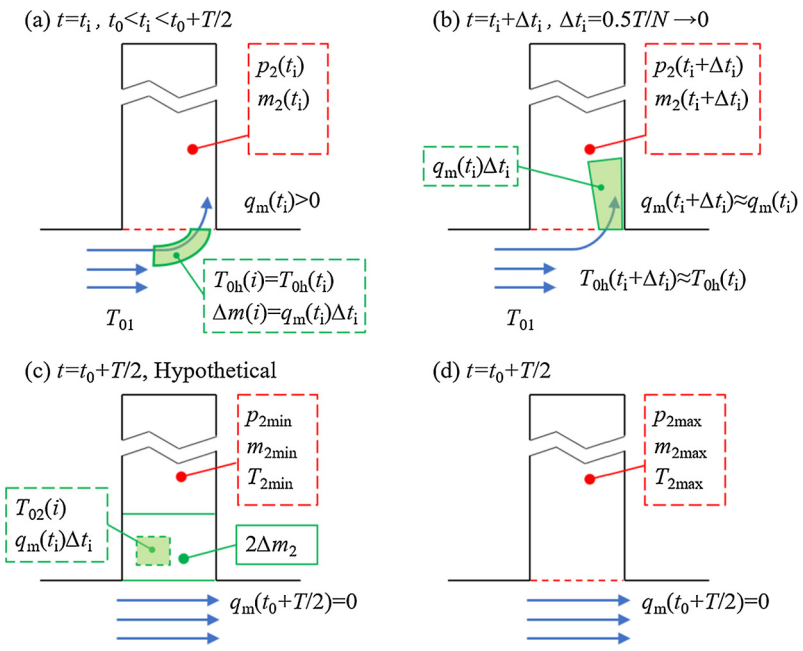

Fig. 16. Schematic of the charge process of the tube.

The stagnation temperature can also characterize the total energy with the c_p nearly unchanged. Equations (4)–(7) can be found in [70] or other books on aerodynamics.

The charge process can be described in Lagrangian view of aerodynamics (the discharge process is similar due to the periodicity). The instantaneous mass flow rate through the pressure sensing hole is $q_m(t_i)$ at $t = t_i$. During a tiny time Δt_i around the time t_i, the outer gas with a mass of $\Delta m(i)$ and a stagnation temperature of $T_{0h}(i)$ flows into the tube and decelerates (see Fig. 16(a)). Note that $\Delta m(i) = q_m(t_i)\Delta t_i$ and $T_{0h}(i) = T_{0h}(t_i)$. At $t = t_0 + \Delta t_i$, this micro mass of gas (the green block in Fig. 16) just flows into the tube entirely and continues decelerating (Fig. 16(b)). At $t = t_0 + T/2$, all the gas, which enters the tube during $t_0 < t < t_0 + T/2$, has decelerated to approximate static state. Equivalently, suppose that each micro mass of inflow gas transfer does not exchange energy with the inner gas until $t = t_0 + T/2$. The stagnation temperature of the particular micro mass $q_m(t_i)\Delta t_i$ is denoted by $T_{02}(i)$ at $t = t_0 + T/2$ (Fig. 16(c)). Then the inflow gas exchange energy with the inner gas, and the temperature in the tube reaches T_{2max}.

The stagnation temperature within the boundary layer varies with the distance from the wall, and the stagnation temperature is lower than that in the main flow, i.e. $T_{0h}(t) < T_{01}$. $T_{0h}(t)$ is in fact mass-averaged stagnation temperature of the gas that flows into the tube. However, $T_{0h}(t)$ for the inflow gas is hard to formulate because the flow field is unsteady. Hence the stagnation temperature of the main flow is chosen as reference. A stagnation temperature ratio, $\alpha(i)$, is introduced to characterize the stagnation enthalpy for the particular micro mass of gas:

$$\alpha(i) = \frac{T_{02}(i)}{T_{0h}(i)}\frac{T_{0h}(i)}{T_{01}} = \frac{T_{02}(i)}{T_{01}} \tag{8}$$

$\alpha(i)$ characterizes the change of stagnation enthalpy before/after the gas flows into the tube. Because the tube wall is adiabatic, the energy transfer happens between the inner gas and the inflow gas. Dividing the charge process into N sections ($N = 501$ in this paper), the maximum temperature can be derived according to conservation of energy:

$$m_{2\,min}c_p\,(T_{2\,max} - T_{2\,min}) = -\sum_{i=0}^{N-1} q_m(t_i)\Delta t_i c_p\,[T_{2\,max} - T_{02}\,(i)] \tag{9}$$

$$T_{2\,max} = \frac{T_{2\,min}\cdot m_{2\,min}}{m_{2\,min}+2\Delta m_2} + \frac{\sum_{i=0}^{N-1}\alpha(i)T_{01}q_m(t_i)\Delta t_i}{m_{2\,min}+2\Delta m_2} \tag{10}$$

Note that $q_m(t_i + \Delta t_i) \approx q_m(t_i)$ and $q_m(t_{i+1}) \neq q_m(t_i)$ because $\Delta t_i \rightarrow 0$. Equation (10) can be rewritten in integral form (sequence number i matches time t_i):

$$T_{2\,max}\cdot(m_{2\,min}+2\Delta m_2) = T_{2\,min}\cdot m_{2\,min} + \int_{t_0}^{t_0+T/2}\alpha(t)T_{01}q_m(t)dt \tag{11}$$

in which m_{2min} is the gas mass in the tube at $t = t_0$. For simplicity, $(m_{2min} + 2\Delta m_2)$ is denoted by m_{2max}, and an equivalent temperature ratio, η, is introduced. η is mass-weighted average $\alpha(t)$ and indicates the stagnation enthalpy change during the entire charge process. It should be noted that η is larger than 1.0 for most cases because a part of energy of the outer airflow transfers to the inflow gas, which results in the stagnation enthalpy increase of the inflow gas. Then equation (11) can be rewritten as:

$$T_{2\,max}\cdot m_{2\,max} - T_{2\,min}\cdot m_{2\,min} = 2\eta T_{01}\Delta m_2 \tag{12}$$

The gas inside the tube is approximately in thermal equilibrium when the tube pressure reaches the maximum or minimum values. Accordingly, Clapeyron equations are established:

$$T_{2\,max}m_{2\,max} = \frac{V}{R}p_{2\,max} \tag{13}$$

$$T_{2\,min}m_{2\,min} = \frac{V}{R}p_{2\,min} \tag{14}$$

in which V is the cubage of the tube, and T_{2max}, T_{2min} are the mass-average gas temperatures inside the tube when the tube pressure reaches p_{2max}, p_{2min}, respectively. The pressure fluctuating amplitude in the tube is approximated as:

$$\Delta p_2 = (p_{2\max} - p_{2\min})/2 \tag{15}$$

Equations (13)–(15) can be substituted into equation (12), i.e.

$$\Delta p_2 = \Delta m_2 \frac{\eta R T_{01}}{V} \tag{16}$$

Considering that the charge segment of $q_m(t)$ is close to a cosine curve (the premise is that a sine pressure signal is input), $q_m(t)$ is approximated as:

$$q_m(t) = q_{\max} \cos[2\pi f\,(t - t_0 - T/4)] \tag{17}$$

in which $t_0 < t < t_0 + T/2$. $q_{\max}$ is the maximum mass flow rate in the charge process. Thus, Δm_2 is approximated as:

$$\Delta m_2 = \frac{1}{2}\int_{t_0}^{t_0+T/2} q_{\max} \cos\left[2\pi f\left(t - t_0 - \frac{T}{4}\right)\right] dt = \frac{q_{\max}}{2\pi f} \tag{18}$$

Substituting equation (18) into equation (16) gives:

$$\Delta p_2 = \frac{q_{\max}}{2\pi f}\frac{\eta R T_1}{V}\left(1 + \frac{\gamma - 1}{2} Ma_1^2\right) \tag{19}$$

According to equation (19), there are six dominant variables for the measuring amplitude - f, Ma_1, $q_{\max}$, η, T_1, V, which are not independent of each other. The complex mechanism of the interaction of these variables is discussed based on CFD results. The following sections present the influence of Mach number, tube configuration and tube cooling, which correspond to the Ma_1, V and η respectively.

4. CFD results and discussion

Systematic numerical simulations have been conducted to further understand the pressure transmission mechanism in compressible flow. Dynamic response characteristics for different Mach numbers are compared and the effect of tap-flow interaction is further analyzed. The influence of tube configuration is studied and the mechanism is explained. Additionally, the tube cooling effect are numerically studied to offer a reference for the supersonic/hypersonic aerodynamic experiments.

4.1. Influence of Mach number

4.1.1. Dynamic response characteristics for different Mach numbers

Numerical simulations were conducted for tube B (see Table 1) for Ma 0.2–4.0, and the transfer functions including mean ratios, amplitude ratios and phase shifts were obtained. CFD results indicate that Mach number has significant influence on the measuring results. For example, the measuring results of 250 Hz input signal for Ma 0.2–4.0 are compared in Fig. 17, which illustrates that the amplitude of $p_2(t)$ in supersonic flow is less than that in subsonic flow, and Δp_2 decreases as Ma increases for $Ma < 2.5$. For supersonic cases, the $p_2(t)$ curve moves up integrally as Ma increases, which results in the increase of $p_{2\text{mean}}$.

The input signal and measuring result are formulated for simplicity:

$$p_1(t) = p_{1\text{mean}} + \Delta p_1 \sin(2\pi f t) \tag{20}$$

$$p_2(t) = p_{2\text{mean}} + \Delta p_2 \sin(2\pi f t - \theta) \tag{21}$$

θ is the phase shift and ranges 0–180°. There is a relation between θ and the time when the charge process begins:

$$\theta = 2\pi f\,(t_0 + T/4) = 2\pi f t_0 + \pi/2 \tag{22}$$

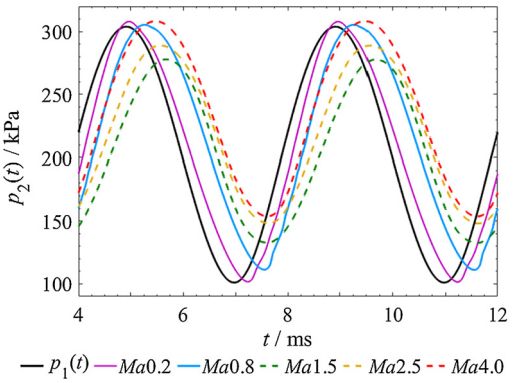

Fig. 17. $p_2(t)$ for different Mach numbers (f = 250 Hz).

The transfer functions for different Mach numbers are shown in Fig. 18. In Fig. 18(a), the mean ratio is not sensitive to Ma in subsonic flow, but the mean ratio increases with Ma in supersonic flow. The mean ratio at Ma = 4.0 increases considerably with f, whereas the mean ratio for lower Mach numbers varies slightly with f. In Fig. 18(b), the amplitude ratio decreases as f increases for all the Mach numbers, thus the short tube is an overdamped pressure measurement system. The amplitude ratio in supersonic flow is much lower than that in subsonic flow for all the frequencies, which has not been reported in existing literature. The $\Delta p_2/\Delta p_1$ for Ma2.5 is lower than that for Ma1.5 and Ma4.0. Hence the relation between $\Delta p_2/\Delta p_1$ and Ma is non-monotonic. In Fig. 18(c), the phase shift increases with f, and varies with Mach number significantly.

In aerodynamic experiments, the difference between the transfer functions in incompressible and compressible flow should be concerned about. If the transfer function for subsonic flow is applied to supersonic flow by mistake, serious error will occur. Nevertheless, quite a few researchers in aerospace field have not paid attention to this problem.

4.1.2. Analysis of the pressure signal at the entrance of the tube

As discussed in section 3, the tube effect includes the tap-flow interaction and the signal distortion near the entrance of the tube. These two aspects correspond to two segments of the pressure transmission: $p_1(t)$ – $p_h(t)$ and $p_h(t)$ – $p_2(t)$. CFD results indicate that Mach number influences $p_1(t)$ – $p_2(t)$ significantly, but the respective sensitivity to Mach number of $p_1(t)$ – $p_h(t)$ and $p_h(t)$ – $p_2(t)$ is not clear. It is necessary to analyze $p_h(t)$ to further understand the pressure transmission mechanism of the measurement system.

$p_h(t)$ curves for different Mach numbers are shown in Fig. 19. The mean and amplitude of $p_h(t)$ varies with Ma, and the $p_h(t)$ curve moves up integrally as Ma increases for supersonic cases. The magnitude tendency of $p_h(t)$ is similar to that of $p_2(t)$ in Fig. 17, but $p_h(t)$ is not a sine signal. Hence the amplitude spectral density of $p_h(t)$ was obtained by fast Fourier transform (Fig. 20). It is clear that the zero-frequency component of $p_h(t)$ increases as Ma increases in supersonic flow. In addition, the high frequency components (500 Hz and 750 Hz) in supersonic flow are larger than that in subsonic flow, which is caused by the disturbed compressible shear flow [60] and the unsteadiness of the separation region [68,69] at the tube entrance in supersonic flow.

Based on the amplitude spectral density of $p_h(t)$, pressure transmission characteristics of $p_1(t)$ – $p_h(t)$ and $p_h(t)$ – $p_2(t)$ for different Ma were obtained to quantify the two aspects of the tube effect. The 250 Hz and 500 Hz input signal cases are analyzed respectively, and only the first order component is considered in the amplitude ratio calculation. Fig. 21(a) illustrates that the $p_{h\text{mean}}/p_{1\text{mean}}$ and $p_{2\text{mean}}/p_{h\text{mean}}$ in supersonic flow are dif-

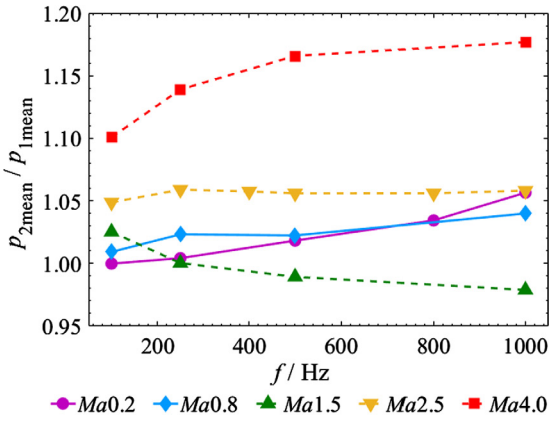

(a) Mean ratios.

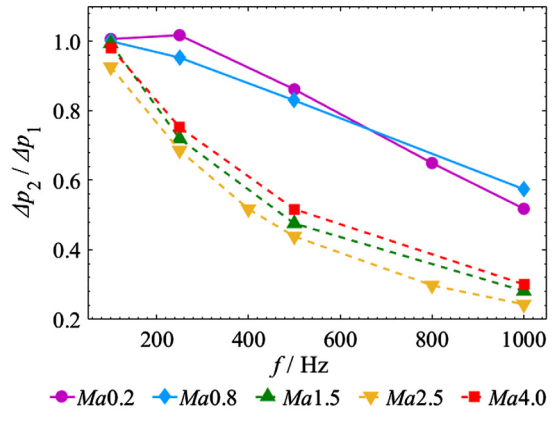

(b) Amplitude ratios.

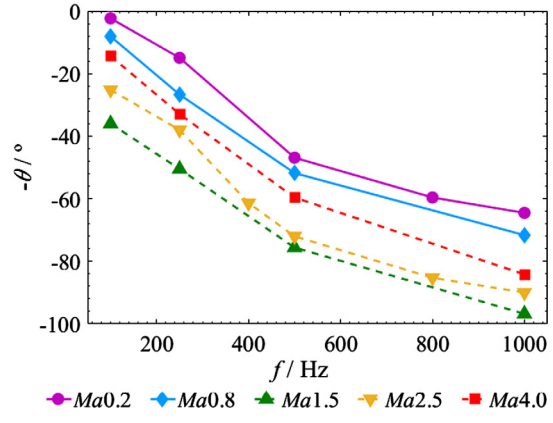

(c) Phase shifts.

Fig. 18. Dynamic response characteristics for different Mach numbers.

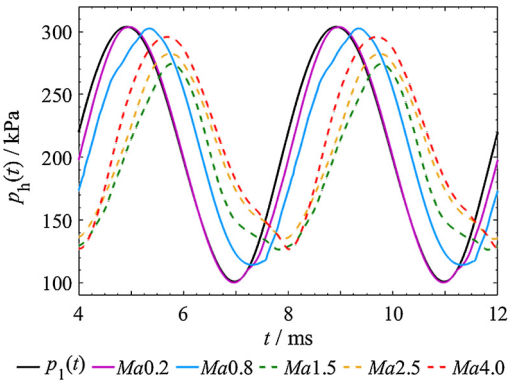

Fig. 19. $p_h(t)$ for different Mach numbers (input f = 250 Hz).

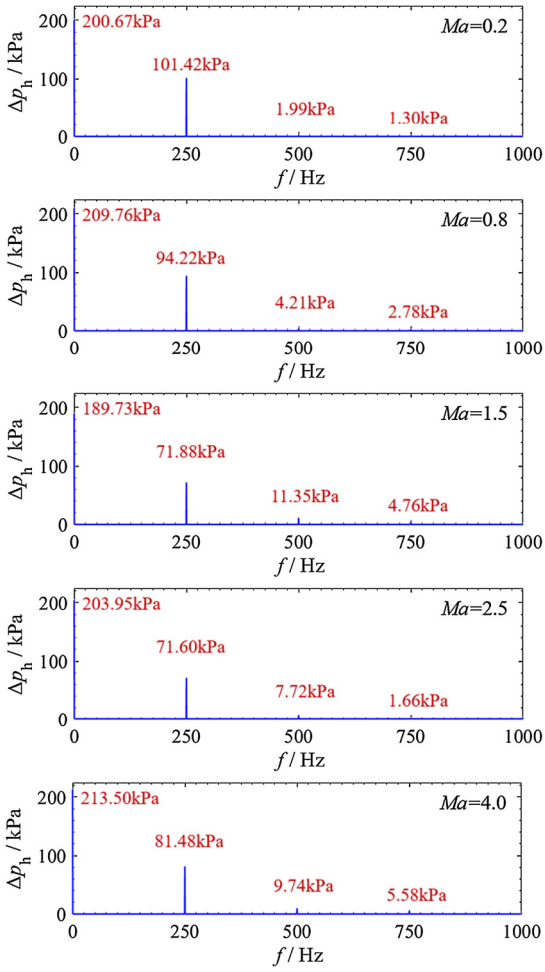

Fig. 20. Amplitude spectral density of $p_h(t)$ (input f = 250 Hz).

ferent with that in subsonic flow. There is a inflection point of the mean ratio at Ma = 0.8, which may be related with the transonic flow at the entrance of the tube. In supersonic flow, p_{hmean}/p_{1mean} increases significantly as Ma increases, which is caused by the higher stagnation pressure of higher Ma flow, whereas p_{2mean}/p_{hmean} changes little as Ma changes. Hence the mean pressure difference between $p_1(t)$ and $p_2(t)$ is mainly determined by the tap-flow interaction at the entrance of the tube. In Fig. 21(b), $\Delta p_{hmean}/\Delta p_{1mean}$ is affected by Ma significantly, whereas $\Delta p_{2mean}/\Delta p_{hmean}$ is less sensitive to Ma, i.e. the signal distortion in the tube is less sensitive to Ma. Nevertheless, both the tap-flow interaction and the internal signal distortion are affected by Ma. These two aspects of the tube effect are not independent of each other.

In fact, $p_h(t)$ is a result of the dynamic interaction between the flow field inside and outside the tube, and the relations $p_1(t)$ – $p_h(t)$ and $p_h(t)$ – $p_2(t)$ are coupled. Hence $p_h(t)$ cannot be calculated from $p_1(t)$ simply, i.e. $p_1(t) \rightarrow p_h(t)$ is not feasible. If the traditional analysis frame in incompressible flow is used based on the hypothesis that $p_1(t)$ – $p_h(t)$ and $p_h(t)$ – $p_2(t)$ can be uncoupled, the tube dynamic response should be obtained by $p_1(t) \rightarrow p_h(t)$ and $p_h(t) \rightarrow p_2(t)$. Then two problems need to be solved. Firstly, $p_h(t)$ is related with the detailed flow structure. There are supersonic shear flow and shock wave-boundary layer interaction at the

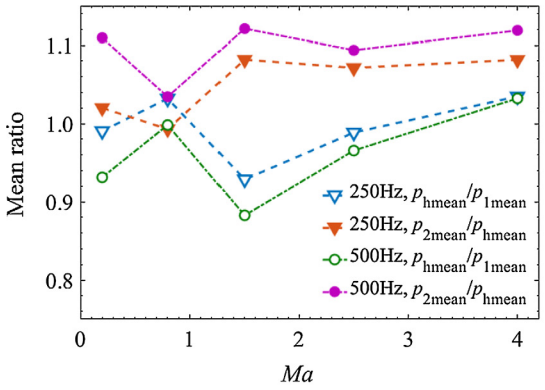

(a) Mean ratios for different Mach numbers.

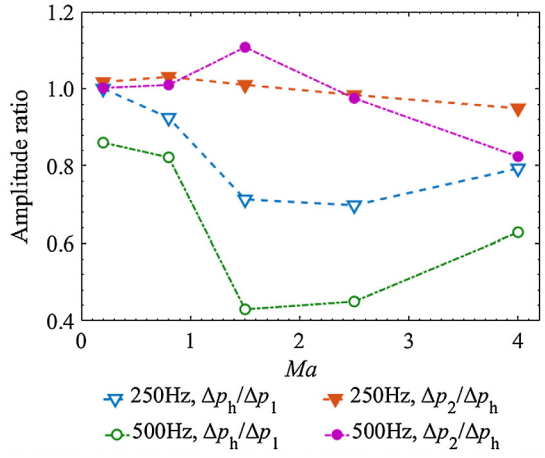

(b) Amplitude ratios for different Mach numbers.

Fig. 21. Pressure transmission characteristics of $p_1(t) - p_h(t)$ and $p_h(t) - p_2(t)$.

entrance of the tube, and the pressure distribution at the entrance section is inhomogeneous, which makes it difficult to estimate the mass-averaged or area-averaged $p_h(t)$ without CFD tools. Secondly, the most signal distortion in the tube happens within the thin tube (see Fig. 12), which is also resulted from the flow structure and difficult to formulate. Therefore, the mechanism of pressure transmission in compressible flow is explained in another frame.

4.1.3. Pressure transmission mechanism

The transmission mechanism of amplitude can be explained based on the model in section 3.3. The amplitude of $p_2(t)$ is determined by the mass flow rate and the stagnation enthalpy change according to equation (19). Hence a conceptual ideal measurement system can be introduced to characterize the amplitude ratio of a given tube. For the ideal measurement system, the mass flow rate and the stagnation temperature ratio are suitable so that the measuring pressure amplitude is equal to the input value Δp_1. Hence the equation (19) can be rewritten as:

$$\Delta p_1 = \frac{q_{1\max}}{2\pi f}\frac{\eta_1 R T_1}{V}\left(1+\frac{\gamma-1}{2}Ma_1^2\right) \tag{23}$$

The q_{1max} is the ideal maximum mass flow rate and can be regarded as the "needed" maximum mass flow rate for a given tube at the given conditions. The η_1 is the ideal stagnation temperature ratio. According to equation (23), the q_{1max} can be expressed as:

$$q_{1\max} = 2\pi f \Delta p_1 \frac{V}{\eta_1 R T_1}\left(1+\frac{\gamma-1}{2}Ma_1^2\right)^{-1} \tag{24}$$

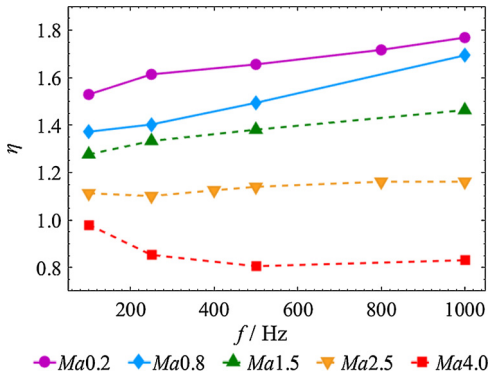

Fig. 22. Equivalent stagnation temperature ratios.

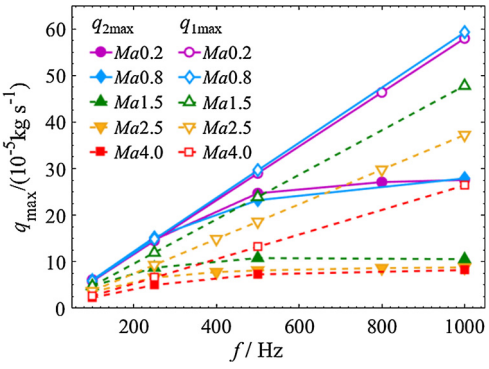

Fig. 23. Real and ideal maximum mass flow rates.

Equation (24) indicates that the q_{1max} is proportional to f, Δp_1 and V (with the hypothesis that η_1 is not sensitive to f, Δp_1 and V). Additionally, q_{1max} decreases as Ma increases. The $\Delta p_2/\Delta p_1$ for a real tube can be approximated as the amplitude ratio of the real tube and the corresponding ideal tube based on equation (19) and (23):

$$\frac{\Delta p_2}{\Delta p_1} = \frac{q_{2\max}}{q_{1\max}}\frac{\eta_2}{\eta_1} \tag{25}$$

According to CFD results, the tube D and E can be regarded as the ideal measurement system (Fig. 30), and the stagnation temperature ratios of the nonideal tubes are close to that of tube D and E. Hence the η_2/η_1 can be approximated as 1.0, and the amplitude ratios can be simply characterized by the q_{2max}/q_{1max}.

The equivalent stagnation temperature ratios under different conditions in Fig. 22 are calculated based on CFD results according to equation (19). η is sensitive to the Mach number, but not sensitive to the frequency. η decreases as Ma increases, which illustrates that the stagnation enthalpy increment in the charge process reduces because of the compressible effect.

The real and ideal maximum mass flow rates are compared in Fig. 23. The q_{2max} is obtained according to equation (24). The q_{1max} is calculated with the η_1 fixed at the value of η_2 at $f = 250$ Hz for simplicity. As shown in Fig. 23, the q_{1max} is not sensitive to Ma in subsonic flow, but the q_{1max} decreases as Ma increases in supersonic flow. The q_{2max} reaches an upper limit as f exceeds a certain value, whereas the q_{1max} ("needed" maximum mass flow rate) is proportional to f. As f increases, q_{2max}/q_{1max} decreases and η_2 changes slightly, which makes the $\Delta p_2/\Delta p_1$ decreases according to equation (25). In supersonic flow, q_{2max} further deviates from q_{1max} and η_2 is less. Therefore, $\Delta p_2/\Delta p_1$ in supersonic flow is significantly less than that in subsonic flow. Hence the constraint of q_{2max} is the decisive factor to the amplitude ratio.

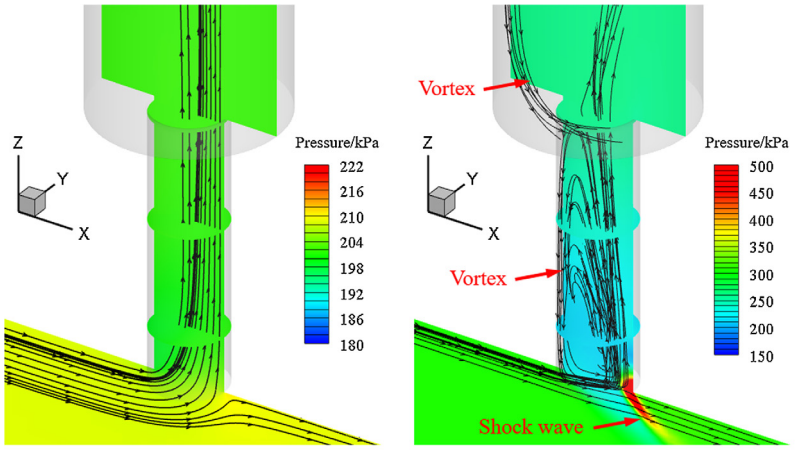

(a) Charge process (Ma = 0.2) (b) Charge process (Ma = 2.5)

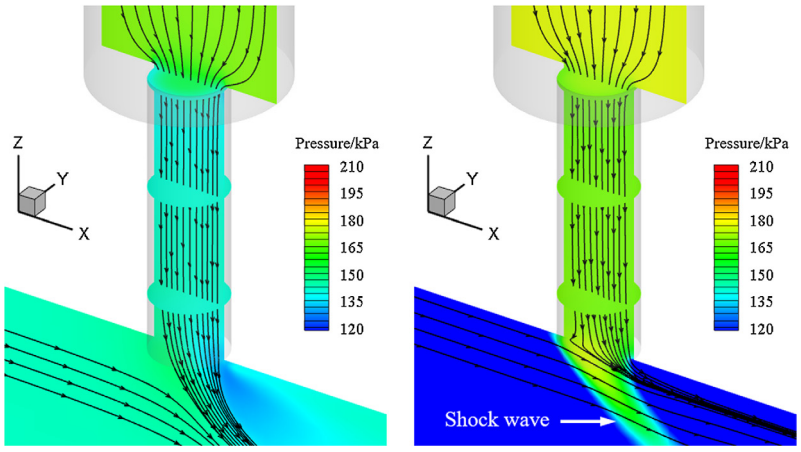

(c) Discharge process (Ma = 0.2) (d) Discharge process (Ma = 2.5)

Fig. 24. Pressure distribution when charging/discharging (f = 250 Hz).

The $q_{2\max}$ is affected by the flow structure. As shown in Fig. 24(a), the inflow streamline distribution is relatively uniform at the entrance of the tube, though the inflow streamlines are slightly affected by the Ma0.2 main flow. In Fig. 24(b), most of the inflow streamlines are close to the $+x$ side of the thin tube and a massive vortex is induced, which indicates that most of the inflow gas is from the shear layer rather than the main flow. The shear flow at the entrance of the tube impacts on the tube wall and causes a high-pressure region at the trailing edge of the pressure sensing hole in the charge process, therefore the main flow is blocked out of the tube. As a result, the inflow mass flow rate is constrained in compressible flow.

The η is also related to the flow structure. The inflow gas loses part of mechanical energy because of the shock wave and vortex in Fig. 24(b), and the temperature difference at the entrance of the tube causes heat transfer from the inner gas to the outer gas (see Fig. 13(b)). Hence the stagnation enthalpy increment of the inflow gas in compressible flow is less than that in incompressible flow, and the higher Ma causes more stagnation enthalpy loss. Consequently, the η decreases as Ma increases.

Fig. 24(c) and (d) illustrate that the outflow streamlines distribution is uniform at the entrance of the tube, whereas the outflow gas is affected by the main flow more seriously in compressible flow. A shock wave is induced at the entrance of the tube in supersonic flow, which diminishes the pressure difference between the outflow gas and the main flow. Hence the outflow gas is blocked and the outflow mass flow rate is constrained.

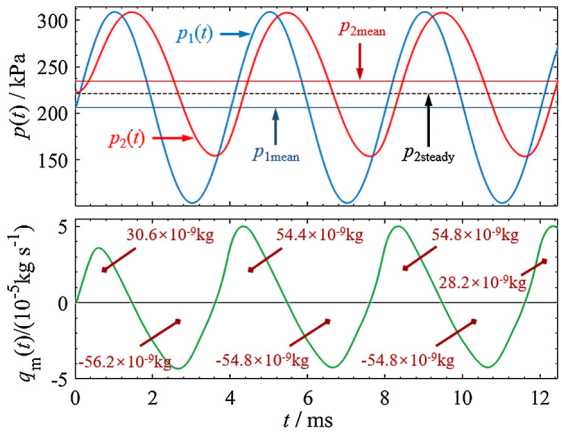

Fig. 25. Correspondence between $p_2(t)$ and $q_m(t)$ (Ma4.0, f = 500 Hz).

The transmission of mean pressure is affected by the flow structure. Fig. 25 shows the $p_1(t)$, $p_2(t)$ and $q_m(t)$ in the start process of the flow field, and the inflow/outflow mass is obtained by the integral of $q_m(t)$. The $p_2(t)$ at t = 0 is the initial pressure in the tube, which is named $p_{2\text{steady}}$. The $p_{2\text{steady}}$ is higher than $p_{1\text{mean}}$ in high Mach flow because the shear layer interacts with the tube wall and makes the pressure at the entrance higher than $p_{1\text{mean}}$. The measuring steady pressure in subsonic flow is also higher than the true value [20,21,23], but the error is less than that in super-

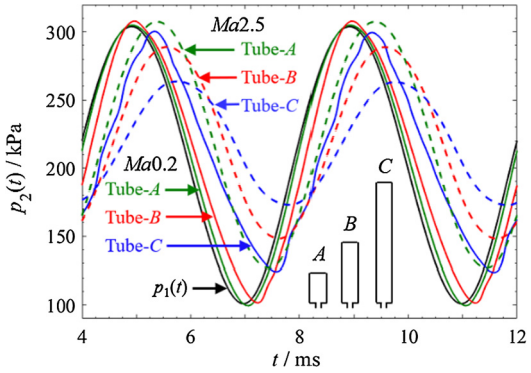

Fig. 26. $p_2(t)$ for different l_2 (f = 250 Hz, Ma0.2 and Ma2.5).

sonic flow. $p_2(t)$ begins to rise at $t = 0$, and the rise of $p_2(t)$ is slower than that of $p_1(t)$ because the inflow mass flow rate is constrained. Then $p_2(t)$ begins to drop from the $p_{2\max}$, which is close to the $p_{1\max}$. The outflow mass is less than the needed value because of the tap-flow interaction, therefore $p_{2\min}$ is much higher than $p_{1\min}$.

The equal inflow/outflow mass indicates a dynamic balance of the flow field after the second fluctuating period of $p_2(t)$. At t = 12.464 ms, $p_2(t)$ reaches the $p_{2\text{mean}}$. The net inflowed mass in the three periods of $p_2(t)$ (i.e. the integral of $q_m(t)$ for t = 0–12.464 ms) is 2.2 × 10^{-9} kg rather than 0, which indicates that extra gas is charged into the tube compared with the initial steady flow field. The tap-flow interaction in compressible flow constrains the mass flow rate, especially the outflow mass flow rate, so some of the inflowed gas cannot flow out. The mass deposition causes energy deposition in the tube; therefore, the mean pressure ratio is larger than 1.0.

4.2. Influence of tube configuration in compressible and incompressible flow

Existing researches [5,16] reveal that the configuration of long tubes (l > 400 mm) influence pressure measuring results significantly in incompressible flow. Whereas, the effect of configuration of short tubes (l < 15 mm) is negligible in incompressible flow according to [15]. The influence of short tube configuration in compressible flow has not been studied, and most pressure transmission tubes in supersonic experiments are designed by experience. Hence the influence of d_2 and l_2 was numerically studied, and the pressure transmission mechanism are explained.

4.2.1. Influence of thick tube length

Numerical simulations were conducted for tubes A (l_2 = 20 mm), B (l_2 = 40 mm) and C (l_2 = 80 mm) at Ma0.2 and Ma2.5 to evaluate the influence of l_2. Tube A corresponds to a pressure sensor with a cavity fixed on the wall of models [39,44]. This installation scheme is commonly used in aerodynamic experiments. The $p_2(t)$ curves at 250 Hz are shown in Fig. 26. The $p_2(t)$ for tube A, Ma0.2 and tube B, Ma0.2 are very close to $p_1(t)$, whereas the $p_2(t)$ for tube C, Ma0.2 deviate from $p_1(t)$. For Ma = 2.5, the $p_2(t)$ varies with l_2 significantly. Therefore, the influence of the thick tube length should be considered in both incompressible flow and compressible flow.

The dynamic response characteristics for different thick tube lengths are shown in Fig. 27. In Fig. 27(a), the mean ratio for incompressible flow increases with l_2, whereas the mean ratio for compressible flow is insensitive to l_2. In Fig. 27(b), $\Delta p_2/\Delta p_1$ decreases as l_2 increases in both incompressible flow and compressible flow, which is the same as the results in [2,5,6]. It should be noted that the $\Delta p_2/\Delta p_1$ of tube A at Ma2.5 is about 0.5 at 1000

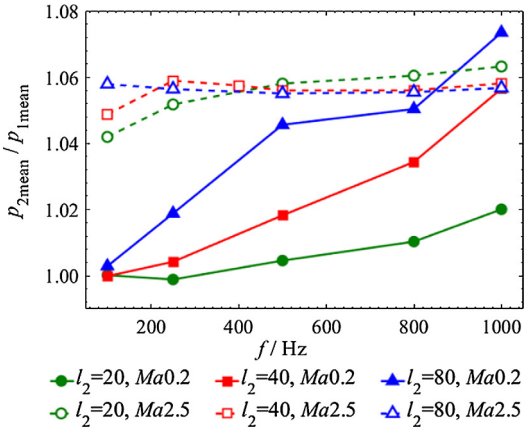

(a) Mean ratios.

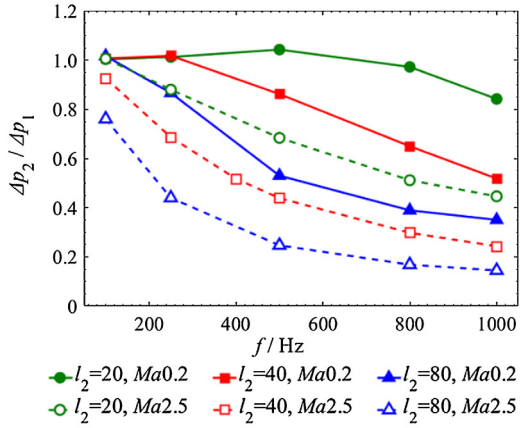

(b) Amplitude ratios.

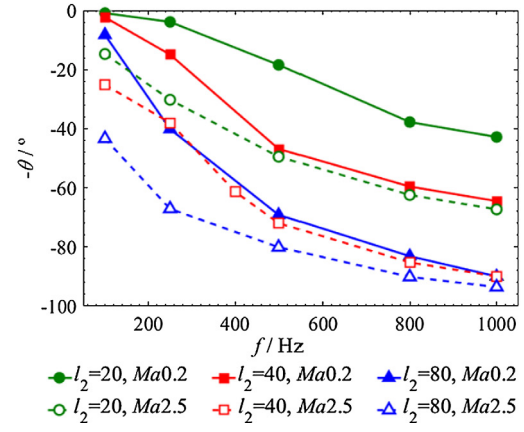

(c) Phase shifts.

Fig. 27. Dynamic response characteristics for different l_2.

Hz, i.e. the uncertainty caused by the transducer cavity is 0.5 Δp_1, but the typical uncertainty of commercially available MEMS sensors is only about 0.001Δp_1 in static calibration. Therefore, the uncertainty caused by the transducer cavity should be considered in high-frequency unsteady pressure measurement in supersonic flow. The influence of l_2 is weak in incompressible flow for f < 200 Hz, whereas the influence of l_2 is considerable in compressible flow for all the frequencies. In Fig. 27(c), the θ increases with l_2

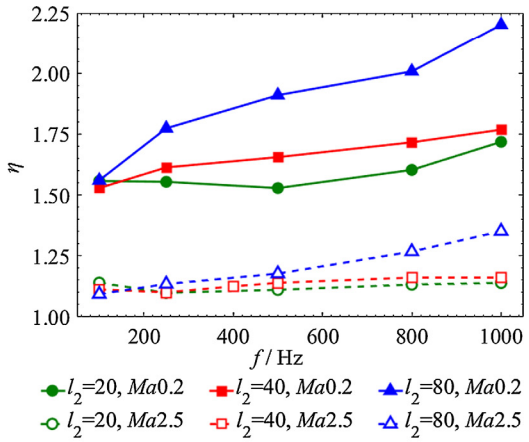

(a) Equivalent stagnation temperature ratios.

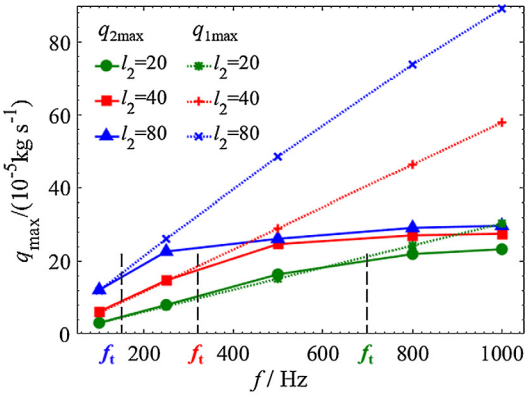

(b) Real and ideal maximum mass flow rates for *Ma*0.2.

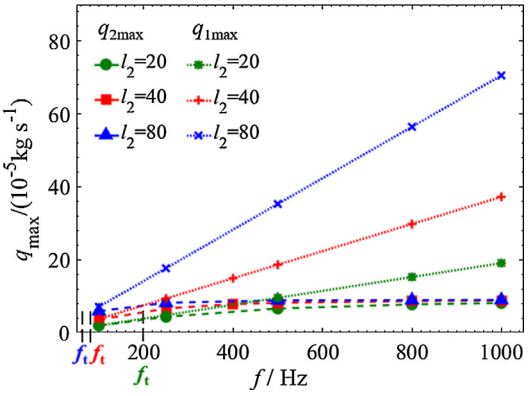

(c) Real and ideal maximum mass flow rates for *Ma*2.5.

Fig. 28. Pressure transmission mechanism analysis for different l_2.

significantly. Fig. 27 illustrates that the transfer functions for short tubes are affected by l_2 under the interference of the cross flow outside the tube. The measurement accuracy drops significantly as l_2 increases.

In [15], a 2.5 mm^3 cavity with a pressure tap was experimentally proved to be suitable for incompressible flow at $f < 256$ Hz. However, the CFD results indicates that a tube configuration suitable for incompressible flow may be unsuitable for compressible flow. For example, the amplitude ratios of tube *A* and *B* are very close to 1.0 at *Ma*0.2, $f < 250$ Hz, whereas the amplitude ratios of tube *A* and *B* deviate from 1.0 at *Ma*0.2, $f > 500$ Hz or *Ma*2.5, $f > 100$ Hz in Fig. 27. Therefore, the tube configuration in [15] should be reevaluated if it is used for higher *Ma* or f.

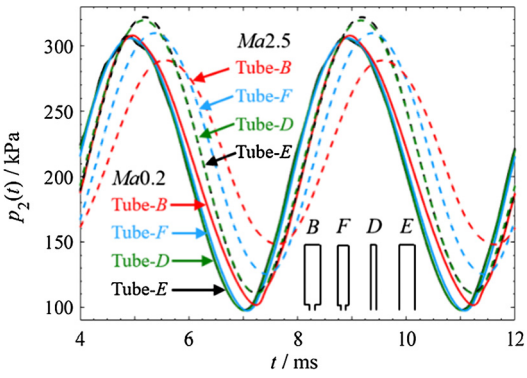

Fig. 29. $p_2(t)$ for different d_2 ($f = 250$ Hz, *Ma*0.2 and *Ma*2.5).

The η, $q_{1\max}$, $q_{2\max}$ for different l_2 are analyzed in Fig. 28. Fig. 28(a) indicates that η varies with l_2 in incompressible flow, whereas η is less sensitive to l_2 in compressible flow. Fig. 28(b) and (c) illustrate that the $q_{1\max}$ increases with l_2, because the tube volume increases with the tube length and the larger $q_{1\max}$ is "needed" (equation (24)). The $q_{2\max}$ increases with l_2 in compressible flow, whereas $q_{2\max}$ is less sensitive to l_2 in compressible flow, i.e. the $q_{2\max}$ is constrained in compressible flow. Hence the $q_{2\max}/q_{1\max}$ decreases as l_2 increases, and the $\Delta p_2/\Delta p_1$ decreases as l_2 increases.

In incompressible flow, the $q_{2\max}$ increases with f in a certain range of f, which makes the $\Delta p_2/\Delta p_1$ close to 1.0. However, the increase of $q_{2\max}$ slows down at a certain f in Fig. 28(b), and the $q_{2\max}$ diverges further from the ideal value $q_{1\max}$ at higher frequencies. Hence the $\Delta p_2/\Delta p_1$ diverges further from 1.0 as f increases in Fig. 27(b). This frequency of the inflection point is named f_t. The f_t for *Ma*0.2 and $l_2 = 20$ mm, 40 mm and 80 mm are about 700 Hz, 320 Hz and 150 Hz according to Fig. 28(b), i.e. f_t decreases as l_2 increases. In compressible flow, the f_t is lower than that in incompressible flow and the $q_{2\max}$ stops increasing at low frequency in Fig. 28(c). The upper limits of the $q_{2\max}$ for different tubes are very close for *Ma*2.5, which indicates that the constraint of mass flow rate is stricter in compressible flow. In brief, the tap-flow interaction at the entrance of the tube is coupled with l_2 in incompressible flow, but uncoupled with l_2 in compressible flow.

4.2.2. Influence of thick tube diameter

Numerical simulations were conducted for tubes *B*, *D*, *E* and *F* at *Ma*0.2 and *Ma*2.5 to evaluate the influence of d_2. *B* ($d_2 = 2$ mm) and *F* ($d_2 = 1.4$ mm) are mixed diameter tubes, and *D* ($d_1 = d_2 = 0.8$ mm) and *E* ($d_1 = d_2 = 1.94$ mm) are straight tubes. As shown in Fig. 29, the measuring results of *E*, *D* and *F* coincide at *Ma*0.2, and the $p_2(t)$ curves are close to $p_1(t)$. The $p_2(t)$ of tube *B* deviate slightly from $p_1(t)$ at *Ma*0.2. At *Ma*2.5, the $p_2(t)$ curves of *E* and *D* moves up integrally and still coincide, whereas the $p_2(t)$ curves of *F* and *B* separate and the amplitudes decrease. The influence of d_2 is more significant in compressible flow.

The dynamic response characteristics are shown in Fig. 30. Fig. 30(a) indicates that the mean ratios of the four tubes increase with f, and the mean ratios in incompressible and compressible flow are close at higher f. Fig. 30(b) illustrates that the amplitude ratios of *D* and *E* are larger than 1.0 at *Ma*0.2, and close to 1.0 at *Ma*2.5. Therefore, the straight tubes *D* and *E* can be regarded as ideal measurement systems in compressible flow. The amplitude ratios of tubes *F* and *B* are less than that of *D* and *E*, i.e. $\Delta p_2/\Delta p_1$ decreases as d_2 increases. Fig. 30(c) illustrates that the phase shifts of straight tubes are less than that of mixed diameter tubes, especially in compressible flow.

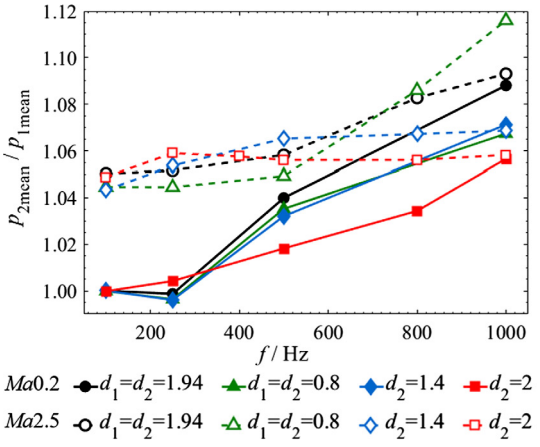

(a) Mean ratios.

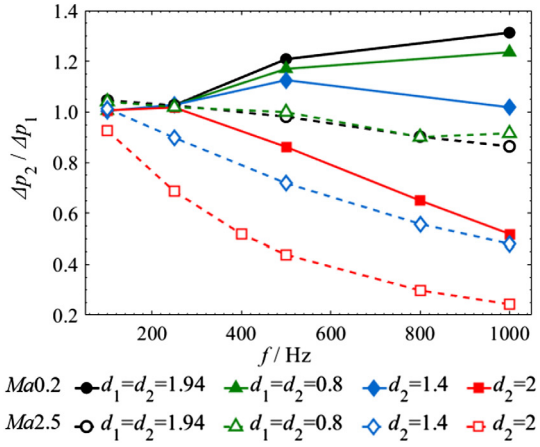

(b) Amplitude ratios.

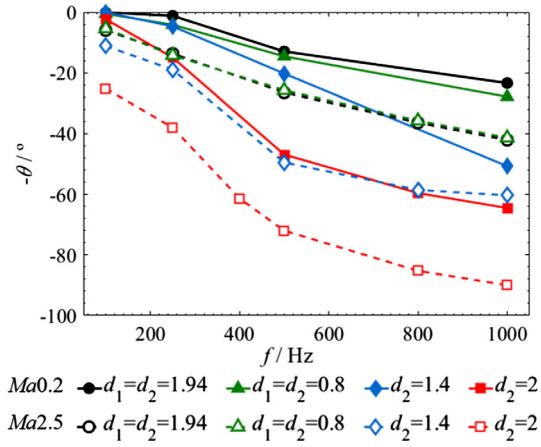

(c) Phase shifts.

Fig. 30. Dynamic response characteristics for different d_2.

The η, q_{1max}, q_{2max} for different d_2 are analyzed in Fig. 31. Fig. 31(a) illustrates that η is not sensitive to d_2 in both incompressible flow and compressible flow. In Fig. 31(b), the q_{2max} of tubes D and F are close to the q_{1max} for 0–1000 Hz, therefore the amplitude ratios of D and F are close to 1.0 at Ma0.2. For $f > 250$ Hz, the q_{2max} of tubes B is less than the q_{1max}, and the q_{2max} of tubes E is larger than the q_{1max}. Therefore, $\Delta p_2/\Delta p_1$ is less than 1.0 for tube B and $\Delta p_2/\Delta p_1$ is larger than 1.0 for tube E at Ma0.2.

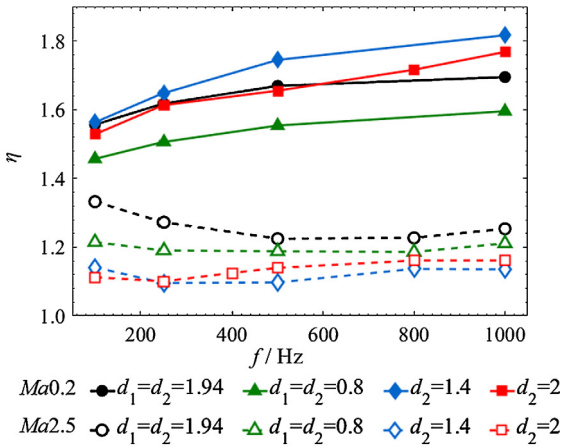

(a) Equivalent stagnation temperature ratios.

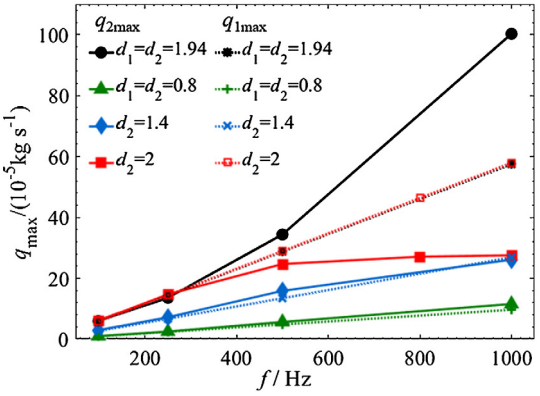

(b) Real and ideal maximum mass flow rates for Ma0.2.

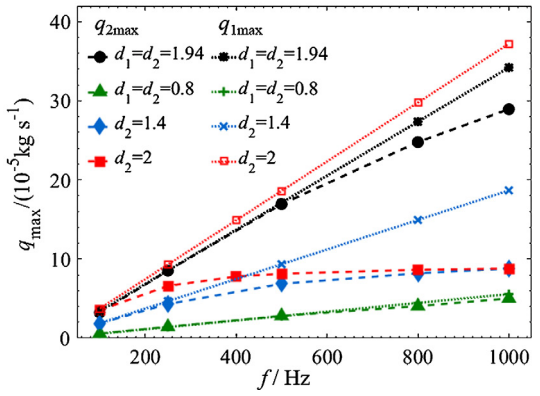

(c) Real and ideal maximum mass flow rates for Ma2.5.

Fig. 31. Pressure transmission mechanism analysis for different d_2.

In Fig. 31(c), the q_{2max} of the straight tubes E and D are close to the q_{1max}, whereas the q_{2max} of the mixed diameter tubes F and B deviate from the q_{1max}. Hence the amplitude ratios of E and D are close to 1.0, and the amplitude ratios of F and B are significantly less than 1.0. Fig. 31(c) also indicates that the q_{2max} of the mixed diameter tubes is insensitive to d_2 in compressible flow.

4.3. Influence of tube cooling

Tube cooling causes the heat transfer between the inflow/outflow gas and the tube wall and affects the measuring results. However, the influence of tube cooling on the measuring results has not

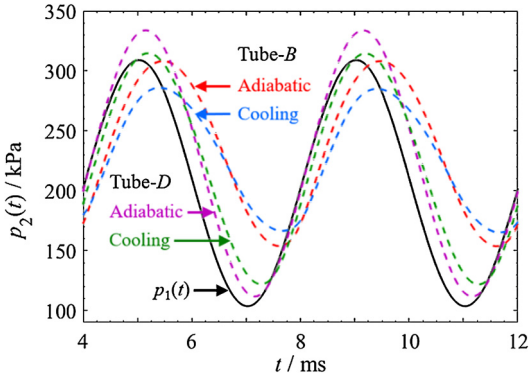

Fig. 32. $p_2(t)$ for adiabatic tube and cooling tube ($f = 250$ Hz, $Ma4.0$).

been studied in existing literature, which hinders the improvement of the measurement accuracy. Hence the influence of tube cooling is numerically studied and the mechanism is explained based on the model in section 3.3. The tube wall temperature was fixed at 300 K (other solid walls were still adiabatic), and the tube wall material was set as steel. The thermal conductivity was calculated based on the kinetic theory. Fig. 32 shows the measuring results of tube B and D with adiabatic/cooled wall. The amplitudes of the cooled tubes reduce clearly compared with the adiabatic tubes. The influence of tube cooling is considerable, and the transfer functions of adiabatic tubes are unsuitable for cooled tubes.

The dynamic response characteristics also indicate the significant influence of tube cooling for both the mixed diameter tube and the straight tube. In Fig. 33(a), the mean ratios of cooled tubes are less than that of adiabatic tubes, but still larger than 1.0. In Fig. 33(b), the amplitude ratios of cooled tubes are about 0.1 less than that of adiabatic tubes. Fig. 33(c) illustrates that tube cooling makes the phase shifts increase. The effect of tube cooling is related to the heat transfer between the inner gas and the tube wall. As shown in Fig. 34, tube cooling results in an unsteady wall heat flux $q_{\text{heat}}(t)$. The positive value of $q_{\text{heat}}(t)$ corresponds to the heat transferred to the tube wall from the inner gas. The maximum heat flux of tube B is larger than that of tube D because the internal surface area of tube B is larger.

With the wall heat flux considered, equation (9) can be rewritten as:

$$m_{2\,\min} c_{\text{p}} \left(T_{2\,\max} - T_{2\,\min}\right) + \sum_{i=0}^{N-1} q_{\text{heat}}\left(t_{\text{i}}\right) \Delta t_{\text{i}}$$
$$= -\sum_{i=0}^{N-1} q_{\text{m}}(t_{\text{i}}) \Delta t_{\text{i}} c_{\text{p}} \left[T_{2\,\max} - T_{02}\left(i\right)\right] \tag{26}$$

The heat transferred to the tube wall in the charge process is denoted $2\Delta H$, which can be written as the integral of $q_{\text{heat}}(t)$:

$$2\Delta H = \int_{t_0}^{t_0+T/2} q_{\text{heat}}\left(t\right) dt \tag{27}$$

It should be noted that $2\Delta H > 0$. Then equation (12) turns into:

$$T_{2\,\max} \cdot m_{2\,\max} - T_{2\,\min} \cdot m_{2\,\min} = 2\eta T_{01} \Delta m_2 - \frac{2\Delta H}{c_{\text{p}}} \tag{28}$$

The amplitude for the cooled tube is:

$$\Delta p_2 = \Delta m_2 \frac{\eta R T_{01}}{V} - \frac{R}{V} \frac{\Delta H}{c_{\text{p}}} = \frac{q_{\max}}{2\pi f} \frac{\eta_{\text{eff}} R T_{01}}{V} \tag{29}$$

in which the η_{eff} is the effective stagnation enthalpy ratio:

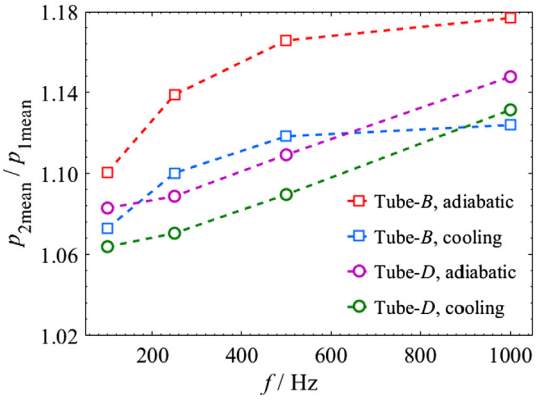

(a) Mean ratios.

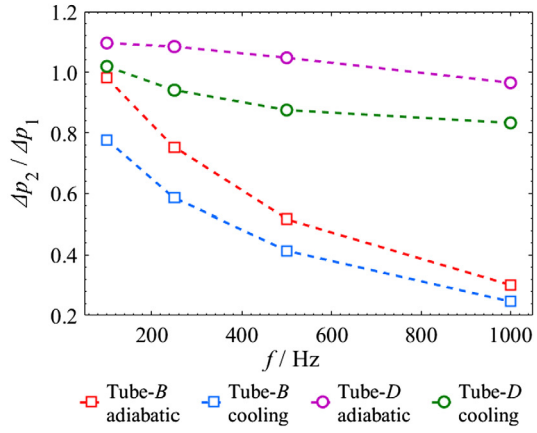

(b) Amplitude ratios.

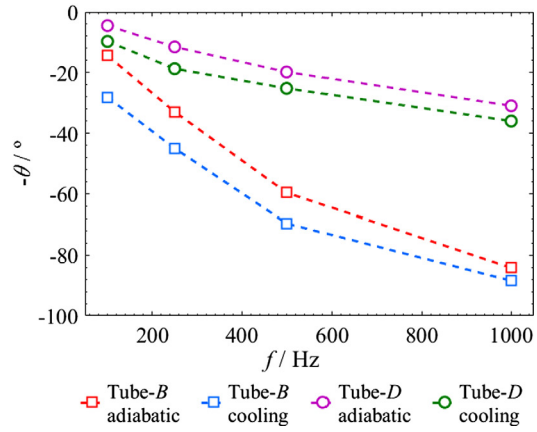

(c) Phase shifts.

Fig. 33. Dynamic response characteristics for the adiabatic and cooling tube.

$$\eta_{\text{eff}} = \eta - \frac{2\pi f}{q_{\max}} \frac{\Delta H}{c_{\text{p}} T_{01}} \tag{30}$$

According to equation (30), η_{eff} is less than η (η corresponds to the adiabatic tube), and η_{eff} decreases as ΔH increases. The physical implication of equation (30) is that the heat transfer between the inner gas and the tube wall reduces the stagnation enthalpy of the inflow gas.

The η and η_{eff} obtained from the CFD results are shown in Fig. 35(a), which proves that η_{eff} is less than η. The difference between η and η_{eff} is more significant for tube D. The reason

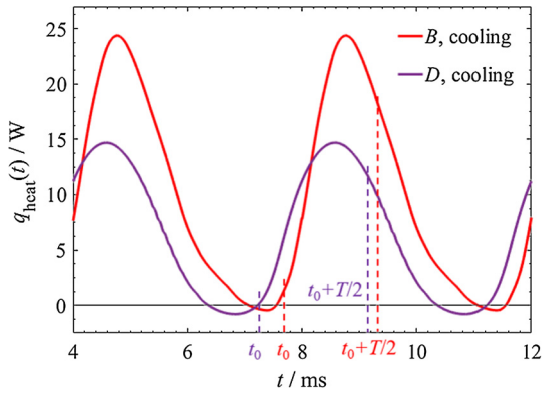

Fig. 34. Wall heat flux for adiabatic tube and cooling tube (f = 250 Hz, Ma4.0).

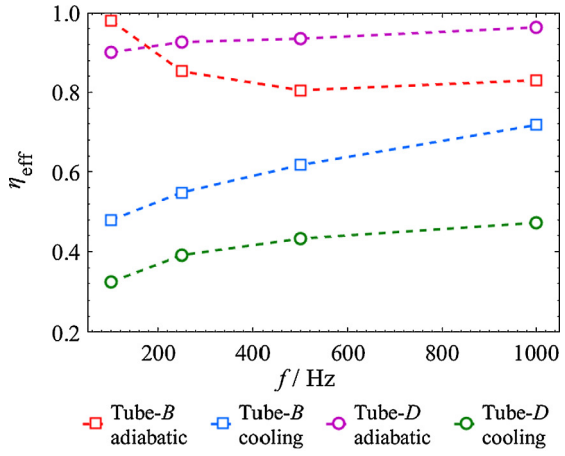

(a) Equivalent stagnation temperature ratios.

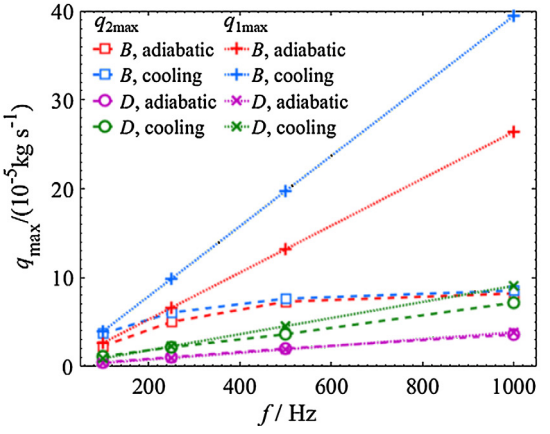

(b) Real and ideal maximum mass flow rates.

Fig. 35. Pressure transmission mechanism analysis for the adiabatic and cooling tube.

is that the specific surface area (internal surface area/cubage) of tube D is larger, and the inflow gas is cooled deeper. Therefore, the $\Delta H/q_{2max}$ is relatively lager for tube D, and $(\eta - \eta_{eff})$ is larger according to equation (30). In Fig. 35(b), the q_{2max} of cooled tubes are larger than that of adiabatic tubes. However, the effect of pressure rise for a unit mass of inflow gas is weakened by the heat transfer in the tube ($\eta_{eff} < \eta$), and larger q_{1max} is needed. Hence the q_{2max}/q_{1max} for cooled tubes deviates further from 1.0, and the amplitude ratios of cooled tubes is less than that of adiabatic tubes.

Table 4
Variables for amplitude ratios estimation.

Tube	Ma_1	η_2	f_t/Hz	f_u/Hz	$q_{2u}/(10^{-5}$ kg s$^{-1})$
A	0.2	1.60	700	>1000	24.0
A	2.5	1.13	200	800	8.10
B	0.2	1.70	320	760	27.5
B	2.5	1.16	80	450	8.75
B	4.0	0.87	120	600	8.21
B (cooled)	4.0	0.60	70	550	8.53
D	4.0	0.93	800	>1000	3.75
D (cooled)	4.0	0.42	160	>1000	7.17

5. Rapid estimation of amplitude ratios

The amplitude is usually more important than the mean and phase shift in aerodynamic experiments. However, it is difficult to give the exact amplitude ratios for compressible flow by theoretical models. On the other hand, the CFD methods based on three-dimensional unsteady calculation needs much computing resource. Hence a database of dominant variables can be established according to CFD results, and the amplitude ratios for different Ma, f and tube configurations can be estimated rapidly.

This estimation method is based on the mechanism that the amplitude ratio is mainly affected by the constraint of the mass flow rate. The amplitude ratio is given based on equation (19):

$$\frac{\Delta p_2}{\Delta p_1} = \frac{q_{2\,max}}{2\pi f}\frac{\eta_2 R T_1}{V \Delta p_1}\left(1 + \frac{\gamma - 1}{2} Ma_1^2\right) \tag{31}$$

The η_2 and q_{2max} are main variables. For simplicity, the η_2 is a constant for the given tube configuration and Mach number. As discussed above, the q_{2max} reaches an upper limit as f increases. Hence the q_{2max} is approximated as a piecewise function of the frequency.

$$q_{2\,max} = \begin{cases} q_{1\,max}, & f < f_t \\ \frac{q_{2u} - q_{2t}}{f_u - f_t}(f - f_t) + q_{2t}, & f_t \le f \le f_u \\ q_{2u}, & f > f_u \end{cases} \tag{32}$$

Tubes A, B and D are chosen to demonstrate the estimation method. The variables under different conditions (Table 4) are obtained based on the CFD results in section 4. The f_u is the frequency at which the q_{2max} reaches the upper limit q_{2u} and stops increasing with f. The η_2, f_t, f_u, q_{2u} of a given tube at different Mach numbers can be obtained from finite data by interpolation. For example, the η_2, f_t, f_u, q_{2u} of tube B at Ma3.2 can be estimated based on interpolation of the data in Fig. 22 and Fig. 23. Considering the highest frequency of the CFD cases in this paper is 1000 Hz, if the f_u exceeds 1000 Hz, the f_u is replaced by 1000 Hz and the q_{2u} is replaced by the q_{2max} at 1000 Hz.

The estimation results are shown in Fig. 36. The estimated amplitude ratios of tubes A and B in incompressible and compressible flow agree with the CFD results in Fig. 36(a). The difference between the estimated amplitude ratios and CFD results is within 0.08 for most cases, which indicates that the estimation method can be used in engineering fields. Fig. 36(b) indicates that the estimation method can distinguish between the amplitude ratios of adiabatic tube and cooled tube. The estimation method also shows some defects. Firstly, the q_{2max} for $f < f_t$ is fixed at q_{1max} in equation (32), but q_{2max} may be larger than q_{1max}. Hence the estimated amplitude ratios for adiabatic tube D deviate from CFD results for $f < f_t$. Secondly, the estimated amplitude ratios for $f_t < f < f_u$ are not accurate enough because the formulations of q_{2max} and η_2 are too simple. In fact, q_{2max} is not linear to f and η_2 varies with f. The formulations of q_{2max} and η_2 as functions of Ma_1, f, l_1, l_2, d_1, d_2 need further study in the future.

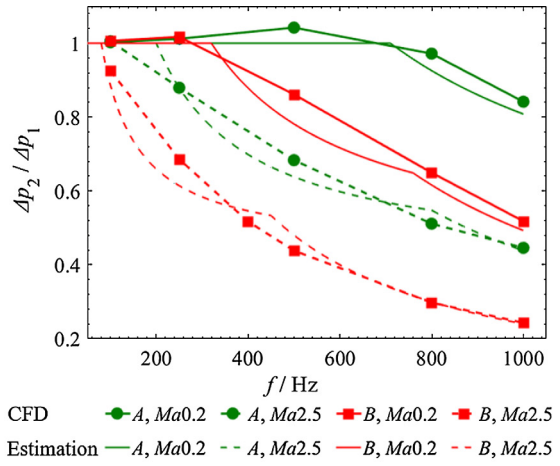

(a) Ma0.2 and Ma2.5.

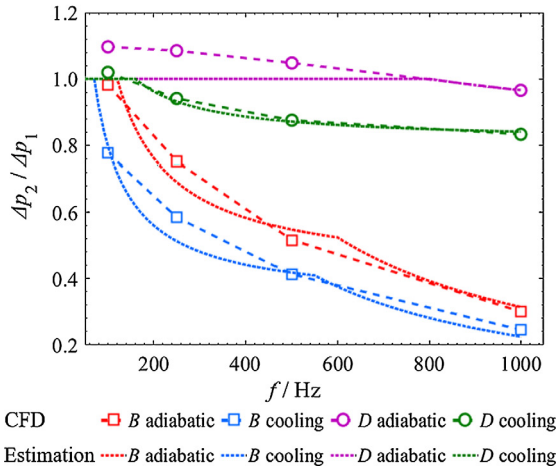

(b) Ma4.0 for adiabatic and cooled tubes.

Fig. 36. Comparison between estimated amplitude ratios and CFD results.

6. Conclusions

The dynamic response of pressure transmission tubes in compressible flow is studied with a novel CFD method in this paper. The flow structure of the tubes is obtained and analyzed. The CFD results indicate that the tube effect in compressible flow includes the tap-flow interaction at the entrance of the tube and the signal damping inside the tube, and the latter is less important for short tubes in compressible flow. As a result of the tap-flow interaction, the pressure signal at the pressure sensing hole $p_h(t)$ is significantly different from the true wall pressure $p_1(t)$, and $p_h(t)$ is hard to predict analytically because of the compressible shear flow, shock wave and boundary layer separation at the pressure tap. Hence the traditional models based on the relation between the measuring pressure signal $p_2(t)$ and $p_h(t)$ is inappropriate to predict the relation between $p_2(t)$ and $p_1(t)$ in compressible flow.

Based on the flow structure of the pressure transmission tubes, a novel simple theoretical model was developed to understand the physical mechanism of the tube dynamic response. The theoretical analysis reveals that the measuring pressure amplitude mainly depends on the mass flow rate through the pressure sensing hole (q_{max}) and the stagnation enthalpy change of the inflow gas in the charge process (η). q_{max} is affected by the Mach number, frequency and tube configuration. η is sensitive to Mach number and tube cooling, but less sensitive to frequency and tube configuration. The mean pressure in the tube is also related to the tap-flow interaction.

The influences of Mach number, tube configuration and tube cooling were numerically studied with CFD method according to the dominant variables in the model. The CFD results indicate that the dynamic response characteristics of a given tube in compressible flow are significantly different from that in incompressible flow. The inflow and outflow gas are considerably affected by the outer high-speed cross flow, as a result, the q_{max} is strictly constrained in compressible flow. In incompressible flow, the tap-flow interaction is negligible and the q_{max} is closer to the ideal value. As f increases, the real maximum mass flow rate reaches an upper limit and stops increasing. The influence of tube configuration is negligible for incompressible flow and low-frequency input signal, but significant for compressible flow and high-frequency signal. The measurement uncertainty caused by the transducer volume (with a magnitude of $0.5\Delta p_1$) is much larger than that caused by the typical pressure sensing element ($0.001\Delta p_1$). Generally, the amplitude ratio decreases as the thick tube length increases, and the amplitude ratio of the straight tube is larger than that of the mixed diameter tube. In addition, it is discovered that the cooled tube wall causes more serious pressure signal damping than the adiabatic tube wall, which is not considered in existing research. Tube cooling can reduce the amplitude ratio by 0.1 in high enthalpy flow. The tube material may also affect the dynamic response characteristics. Materials with special mechanic and thermal properties, such as functionally graded materials [71–74] and high entropy alloys [75,76], can be assessed in the future.

It is difficult to develop an accurate and universal analytical model for compressible flow because of the complex flow structure. Instead, the CFD method is more flexible and suitable for engineering applications. In addition, a method of rapid estimation of amplitude ratios is developed based on the CFD database. The maximum difference between the estimated amplitude ratios and CFD results are about 0.08. It should be noted that the CFD method may need much computing resource. Another possible solution is to develop more robust flush-mount high-temperature sensors to measure the "true" wall pressure directly in high enthalpy airflow.

Declaration of competing interest

The authors declare that they have no known competing financial interests or personal relationships that could have appeared to influence the work reported in this paper.

Acknowledgements

This work is sponsored by the National Natural Science Foundation of China (No. 11672309, 11902325, 11472279).

Appendix A. Convergency of transient calculation

The unsteady numerical simulations with different time step sizes were conducted to verify the convergency of transient calculation. The transient calculation settings are shown in Table A.1. More inner iterations are set for larger time step size to ensure the convergency. In Fig. A.1, the residual of mass equation declines from 7.4×10^{-8} to 1.4×10^{-11} and the residual of z-velocity declines from 1.5×10^{-7} to 4.7×10^{-9} in a time step. The residuals stabilize after about 50 inner iterations of each time step, which indicate the convergency at the corresponding flow time. The $p_2(t)$ curves for different time resolutions coincide in Fig. A.2. Hence the transient calculation settings are appropriate. The $T/1000$ time resolution is chosen considering the computing resource.

Table A.1
Transient calculation settings.

Time resolution	Time step size/s	Sampling rate/kHz	Courant number	Inner iterations
$T/200$	1×10^{-5}	100	10	130
$T/500$	4×10^{-6}	250	10	130
$T/1000$	2×10^{-6}	500	10	100
$T/2000$	1×10^{-6}	1000	10	60

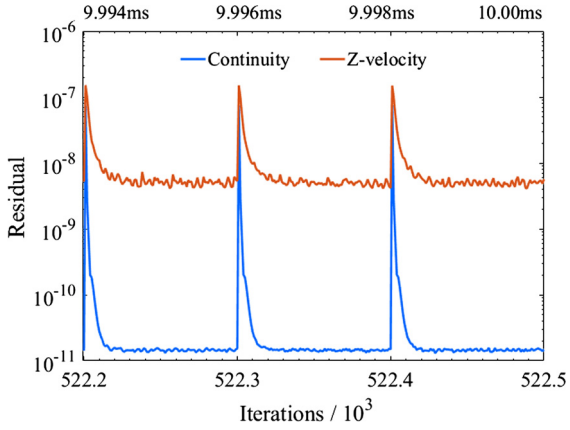

Fig. A.1. Residuals in calculation ($Ma2.5$, $f = 500$ Hz, Time resolution $= T/1000$).

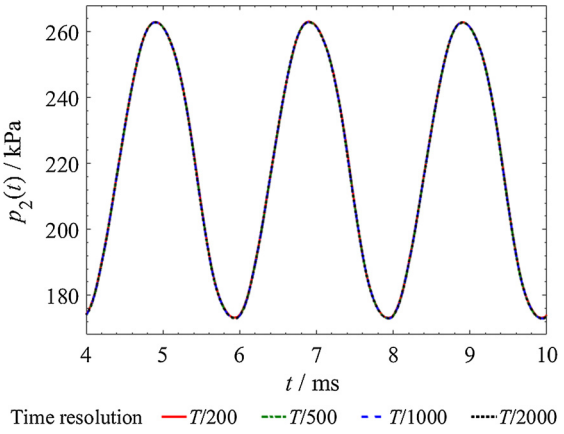

Fig. A.2. $p_2(t)$ for different time resolutions ($Ma2.5$, $f = 500$ Hz).

References

[1] J. Hjelmgren, Dynamic measurement of pressure – a literature survey, SP Report 2002: 34, SP Swedish National Testing and Research Institute, 2002.

[2] B.F. Hall, T. Povey, A practical model for pressure probe system response estimation (with review of existing models), Meas. Sci. Technol. 29 (2018) 045301, https://doi.org/10.1088/1361-6501/aaa58f.

[3] C. Antonini, G. Persico, A.L. Rowe, Prediction of the dynamic response of complex transmission line systems for unsteady pressure measurements, Meas. Sci. Technol. 19 (2008) 125401, https://doi.org/10.1088/0957-0233/19/12/125401.

[4] S.A. Whitmore, B. Fox, Improved accuracy, second-order response model for pressure sensing systems, J. Aircr. 46 (2009) 491–500, https://doi.org/10.2514/1.36262.

[5] H. Bergh, H. Tijdeman, Theoretical and experimental results for the dynamic response of pressure measuring systems, NLR Technical Report F.238, Netherlands Aerospace Centre, Amsterdam, 1965.

[6] J. Kutin, A. Svete, On the theory of the frequency response of gas and liquid pressure measurement systems with connecting tubes, Meas. Sci. Technol. 29 (2018) 125108, https://doi.org/10.1088/1361-6501/aae884.

[7] H.P.A.H. Irwin, K.R. Cooper, R. Girard, Correction of distortion effects caused by tubing systems in measurements of fluctuating pressures, J. Ind. Aerodyn. 5 (1979) 93–107.

[8] G. Paniagua, R. Dénos, Digital compensation of pressure sensors in the time domain, Exp. Fluids 32 (2002) 417–424, https://doi.org/10.1007/s003480100355.

[9] S.A. Whitmore, M.D. Wilson, S.D. Eilers, Novel technique for reconstructing high-frequency transient rocket chamber-pressure measurements, J. Spacecr. Rockets 47 (2010) 427–441, https://doi.org/10.2514/1.46386.

[10] A. Gatto, K.P. Byrne, N.A. Ahmed, R.D. Archer, Mean and fluctuating pressure measurements over a circular cylinder in cross flow using plastic tubing, Exp. Fluids 30 (2001) 43–46, https://doi.org/10.1007/s003480000133.

[11] A. Fisher, S. Watkins, J. Watmuff, Dynamic calibration of pressure measurement system-an improved method, in: 18th Australasian Fluid Mechanics Conf., Launceston, Australasia, December 2012.

[12] R. Semaan, P. Scholz, Pressure correction schemes and the use of the Wiener deconvolution method in pneumatic systems with short tubes, Exp. Fluids 53 (2012) 829–837, https://doi.org/10.1007/s00348-012-1332-2.

[13] D.H. Kim, J.W. Chang, H.B. Kim, Aerodynamic characteristics of a pitching airfoil through pressure-distortion correction in pneumatic tubing, J. Aircr. 50 (2013) 590–598, https://doi.org/10.2514/1.C031941.

[14] G. Jones, S. Balakrishna, J. DeMoss, S. Goodliff, M. Bailey, Influences of models on the unsteady pressure characteristics of the NASA national transonic facility, in: AIAA Scitech Forum, Kissimmee, January 2015, AIAA 2015-1557.

[15] H. Kozmar, P. Dolinsky, Pressure tap cavity for unsteady aerodynamic pressure measurements, Measurement 132 (2019) 282–291, https://doi.org/10.1016/j.measurement.2018.09.056.

[16] P. Nikoueeyan, M.D. Hind, J. Strike, M. Singh, J.W. Naughton, S. Keeter, M. Dahland, Characterization of unsteady pressures on a blunt trailing edge using a direct-mount pressure scanner, in: AIAA Scitech Forum, San Diego, January 2019, AIAA 2019-1827.

[17] R. Gejji, I. Walters, S. Beard, A. Lemcherfi, S. Sardeshmukh, S. Heister, C. Slabaugh, Transducer installation effects on pressure measurements in pressure gain combustion devices, in: AIAA Aerospace Sciences Meeting, Kissimmee, January 2018, AIAA 2018-0158.

[18] M.L. Fotia, J. Hoke, F. Schauer, Experimental study of the response of capillary tube attenuated pressure measurements to high amplitude, non-linear forcing, in: AIAA Aerospace Sciences Meeting, Kissimmee, January 2018, AIAA 2018-0634.

[19] F.C. Sahin, J. Schiffmann, Dynamic pressure probe response tests for robust measurements in periodic flows close to probe resonating frequency, Meas. Sci. Technol. 29 (2018) 025301, https://doi.org/10.1088/1361-6501/aa9cf4.

[20] R. Shaw, The influence of hole dimensions on static pressure measurements, J. Fluid Mech. 7 (4) (1960) 550–564, https://doi.org/10.1017/S0022112060000281.

[21] R.E. Franklin, J.M. Wallace, Absolute measurements of static-hole error using flush transducers, J. Fluid Mech. 42 (1) (1970) 33–48, https://doi.org/10.1017/S0022112070001052.

[22] H. Zogg, H. Thomann, Errors in static pressure measurements due to protruding pressure taps, J. Fluid Mech. 54 (3) (1972) 489–494, https://doi.org/10.1017/S0022112072000825.

[23] C. Ducruet, A. Dyment, The pressure-hole problem, J. Fluid Mech. 142 (3) (1984) 251–267, https://doi.org/10.1017/S0022112084001099.

[24] G. Dell'Era, M. Mersinligil, J. Brouckaert, Assessment of unsteady pressure measurement uncertainty-part I: single sensor probe, J. Eng. Gas Turbines Power 138 (4) (2016) 041601, https://doi.org/10.1115/1.4031371.

[25] G. Dell'Era, M. Mersinligil, J. Brouckaert, Assessment of unsteady pressure measurement uncertainty-part II: virtual three-hole probe, J. Eng. Gas Turbines Power 138 (4) (2016) 041602, https://doi.org/10.1115/1.4031373.

[26] S.Z. Pinckney, A short static-pressure probe design for supersonic flow, NASA-TN-D-7978, NASA, 1975.

[27] T.D. Norum, J.M. Seiner, Measurements of mean static pressure and far-field acoustics of shock-containing supersonic jets, NASA-TM-84521, NASA, 1982.

[28] A.R. Porro, Pressure probe designs for dynamic pressure measurements in a supersonic flow field, NASA/TM-2001-211096, 2001.

[29] A. Bouhanguel, P. Desevaux, M. Khan, CFD design study of a pressure probe for centerline static pressure measurement in supersonic ejectors, Int. J. Turbo Jet-Engines 36 (1) (2016) 107–112, https://doi.org/10.1515/tjj-2016-0059.

[30] A. Bouhanguel, P. Desevaux, M. Khan, Development and testing of a pressure probe for centerline static pressure measurement in supersonic nozzles and ejectors, Instrum. Sci. Technol. 46 (3) (2018) 245–252, https://doi.org/10.1080/10739149.2017.1379417.

[31] T. Reagan, J.R. Underbrink, J. Meloy, M. Sheplak, Fabrication and characterization of a flush-mount MEMS piezoelectric dynamic pressure sensor and associated package for aircraft fuselage arrays, in: AIAA Aerospace Sciences Meeting, Grapevine, January 2017, AIAA 2017-0477.

[32] A. Naples, A. Knisely, J. Hoke, F. Schauer, Infinite line pressure probe and flush transducer measurements in a rotating detonation engine channel, in: AIAA Scitech Forum, San Diego, January 2019, AIAA 2019-2022.

[33] X. Jiang, K. Kim, S. Zhang, J. Johnson, G. Salazar, High-temperature piezoelectric sensing, Sensors 14 (2014) 144–169, https://doi.org/10.3390/s140100144.

[34] R.S. Okojie, D. Lukco, C.W. Chang, E. Savrun, Characterization of silicon carbide pressure sensors at 800 °C, NASA GRC-E-DAA-TN67030, 2019.

[35] A. Ned, R. Okojie, A. Kurtz, 6H-SiC pressure sensor operation at 600 °C, in: 4th International High Temperature Electronics Conference, 1998.

[36] F. Masheeb, S. Stefanescu, A. Ned, A. Kurtz, G. Beheim, Leadless sensor packaging for high temperature applications, in: Proceedings of the IEEE Micro Electro Mechanical Systems, 2002, pp. 392–395.
[37] M. Davis, M. Castellucci, M. Palmer, E. Marineau, A miniature, high temperature, high frequency fiber optic pressure sensor for scramjet flow characterization, in: 50th AIAA Aerospace Sciences Meeting Including the New Horizons Forum and Aerospace Exposition, Nashville, January 2012, AIAA 2012-0858.
[38] M. Mersinligil, J. Brouckaert, J. Desset, Unsteady pressure measurements with a fast response cooled probe in high temperature gas turbine environments 133 (8) (2011) 081603, https://doi.org/10.1115/1.4002276.
[39] F.Q. Zhong, L.W. Cheng, H.B. Gu, X.Y. Zhang, Experimental study of flame characteristics of ethylene and its mixture with methane and hydrogen in supersonic combustor, Aerosp. Sci. Technol. 86 (2019) 775–781, https://doi.org/10.1016/j.ast.2019.01.039.
[40] G.Y. Zhao, M.B. Sun, J.S. Wu, X.D. Cui, H.B. Wang, Investigation of flame flashback phenomenon in a supersonic crossflow with ethylene injection upstream of cavity flameholder, Aerosp. Sci. Technol. 87 (2019) 190–206, https://doi.org/10.1016/j.ast.2019.02.018.
[41] D.G. Ferguson, P.C. Ivey, Unsteady pressure measurement in a high temperature environment using water cooled fast response pressure transducers, in: ASME International Gas Turbine and Aeroengine Congress and Exposition, Houston, 1995, 95-GT-345.
[42] D.G. Ferguson, P.C. Ivey, A high temperature assessment of air-cooled unsteady pressure transducers, 97-GT-6, in: ASME International Gas Turbine and Aeroengine Congress and Exposition, Orlando, 1997.
[43] N.T. Lagen, J.M. Seiner, Evaluation of water cooled supersonic temperature and pressure probes for application to 2000 F flows, NASA-TM-102612, NASA, 1990.
[44] L.J. Yue, Y.N. Jia, X. Xu, X.Y. Zhang, P. Zhang, Effect of cowl shock on restart characteristics of simple ramp type hypersonic inlets with thin boundary layers, Aerosp. Sci. Technol. 74 (2018) 72–80, https://doi.org/10.1016/j.ast.2017.12.018.
[45] M. Farahani, A. Daliri, J.S. Younsi, Supersonic inlet buzz detection using pressure measurement on wind tunnel wall, Aerosp. Sci. Technol. 86 (2019) 782–793, https://doi.org/10.1016/j.ast.2019.02.002.
[46] C.P. Wang, C. Cheng, K. Cheng, L.S. Xue, Unsteady behavior of oblique shock train and boundary layer interactions, Aerosp. Sci. Technol. 79 (2018) 212–222, https://doi.org/10.1016/j.ast.2018.05.054.
[47] Y. Meng, H.B. Gu, J.H. Zhuang, W.M. Sun, Z.B. Gao, H. Lian, L.J. Yue, X.Y. Chang, Experimental study of mode transition characteristics of a cavity-based scramjet combustor during acceleration, Aerosp. Sci. Technol. 93 (2019) 105316, https://doi.org/10.1016/j.ast.2019.105316.
[48] X. Zhang, L.J. Yue, T.L. Huang, Q.F. Zhang, X.Y. Zhang, Numerical investigation of mode transition and hysteresis in a cavity-based dual-mode scramjet combustor, Aerosp. Sci. Technol. 94 (2019) 105420, https://doi.org/10.1016/j.ast.2019.105420.
[49] L.L. Gao, G. Yang, W.J. Li, B.R. Li, Measurement of mass flow rate and evaluation of heat transfer coefficient for high-pressure pneumatic components during charge and discharge processes, Flow Meas. Instrum. 45 (2015) 391–403, https://doi.org/10.1016/j.flowmeasinst.2015.08.006.
[50] E. Lavante, H. Kaya, F. Winzösch, S. Brinkhorst, B. Mickan, Flow structure in critical flow Venturi nozzle and its effect on the flow rate, Flow Meas. Instrum. 44 (2015) 97–106, https://doi.org/10.1016/j.flowmeasinst.2014.12.003.
[51] C. Wang, P.J. Cao, C.H. Li, H.B. Ding, L.h. Cui, Influence of wall roughness on boundary layer transition position of the sonic nozzles, Measurement 139 (2019) 196–204, https://doi.org/10.1016/j.measurement.2019.01.091.
[52] J. Geršla, S. Knoteka, Z. Belligolib, R.P. Dwightb, R.A. Robinsonc, M.D. Coleman, Flow rate measurement in stacks with cyclonic flow – error estimations using CFD modelling, Measurement 129 (2018) 167–183, https://doi.org/10.1016/j.measurement.2018.06.032.
[53] B. Wang, Y.H. Du, N.Y. Xu, Simulation and experimental verification on dynamic calibration of fuel gear flowmeters, Measurement 138 (2019) 570–577, https://doi.org/10.1016/j.measurement.2019.02.044.
[54] D.C. Wilcox, Turbulence Modeling for CFD, 3rd ed., DCW Industries, Inc., La Canada, 2006, pp. 115–121.
[55] D.O. Davis, M. Vyas, J. Slater, Research on supersonic inlet bleed, in: AIAA Aerospace Sciences Meeting, Nashville, January 2012, AIAA 2012-0272.
[56] J.W. Slater, Improvements in modeling 90-degree bleed holes for supersonic inlets, J. Aircr. 50 (2013) 590–598, https://doi.org/10.2514/1.B34333.
[57] A. Hamed, A. Morell, G. Bellamkonda, Three-dimensional simulations of bleed-hole rows/shock-wave/turbulent boundary-layer interactions, in: AIAA Aerospace Sciences Meeting, Nashville, January 2012, AIAA 2012-0840.
[58] E. Teh, T.I. Shih, Reynolds-averaged simulations of shock-wave/boundary-layer interactions with bleed, in: AIAA Aerospace Sciences Meeting, Grapevine, January 2013, AIAA 2013-0423.
[59] M.B. Eichorn, P.J. Barnhart, D.O. Davis, M. Vyas, J. Slater, Reynolds-averaged simulations of shock-wave/boundary-layer interactions with bleed, in: AIAA Aerospace Sciences Meeting, Grapevine, January 2013, AIAA 2013-0424.
[60] J.P. Dussauge, Gaviglio, The rapid expansion of a supersonic turbulent flow: role of bulk dilatation, J. Fluid Mech. 174 (1987) 81–112, https://doi.org/10.1017/S0022112087000053.
[61] S. Barre, C. Quine, J.P. Dussauge, Compressibility effects on the structure of supersonic mixing layers: experimental results, J. Fluid Mech. 259 (1994) 47–78, https://doi.org/10.1017/S0022112094000030.
[62] A.J. Smits, J.P. Dussauge, Turbulent Shear Layers in Supersonic Flow, 2rd ed., Springer Science and Business Media, Inc., New York, 2006.
[63] W. Huang, Transverse jet in supersonic crossflows, Aerosp. Sci. Technol. 50 (2016) 183–195, https://doi.org/10.1016/j.ast.2016.01.001.
[64] H. Shi, G. Wang, X. Luo, J. Yang, X. Lu, Large-eddy simulation of a pulsed jet into a supersonic crossflow, Comput. Fluids 140 (2016) 320–333, https://doi.org/10.1016/j.compfluid.2016.10.009.
[65] N.J. Williams, T.M. Moeller, R.J. Thompson, Numerical simulations of high frequency transverse pulsed jet injection into a supersonic crossflow, Aerosp. Sci. Technol. 103 (2020) 105908, https://doi.org/10.1016/j.ast.2020.105908.
[66] F. Smith, P. Brighton, P. Jackson, J. Hunt, On boundary-layer flow past two-dimensional obstacles, J. Fluid Mech. 113 (1981) 123–152, https://doi.org/10.1017/S0022112081003431.
[67] D. Smith, A. Smits, The effects of successive distortions on a turbulent boundary layer in a supersonic flow, J. Fluid Mech. 351 (1997) 253–288, https://doi.org/10.1017/S0022112097006988.
[68] P. Dupont, S. Piponniau, J. Dussauge, Compressible mixing layer in shock-induced separation, J. Fluid Mech. 863 (2019) 620–643, https://doi.org/10.1017/jfm.2018.987.
[69] S. Piponniau, J. Dussauge, J. Debiève, P. Dupont, A simple model for low-frequency unsteadiness in shock-induced separation, J. Fluid Mech. 629 (2009) 87–108, https://doi.org/10.1017/S0022112009006417.
[70] J.D. Anderson, Modern Compressible Flow: With Historical Perspective, 3rd ed., McGraw-Hill Companies, Inc., New York, 2003, pp. 23–86.
[71] B. Saleh, J. Jiang, R. Fathi, T. Al-hababi, Q. Xu, L. Wang, D. Song, A. Ma, 30 Years of functionally graded materials: an overview of manufacturing methods, applications and future challenges, Compos., Part B, Eng. 201 (2020) 108376, https://doi.org/10.1016/j.compositesb.2020.108376.
[72] A. Menasria, A. Kaci, A. Bousahla, F. Bourada, A. Tounsi, K. Benrahou, A. Tounsi, E. Adda Bedia, S. Mahmoud, A four-unknown refined plate theory for dynamic analysis of FG-sandwich plates under various boundary conditions, Steel Compos. Struct. 36 (3) (2020) 355–367, https://doi.org/10.12989/scs.2020.36.3.355.
[73] H. Matouk, A. Bousahla, H. Heireche, F. Bourada, E. Bedia, A. Tounsi, S. Mahmoud, A. Tounsi, K. Benrahou, Investigation on hygro-thermal vibration of P-FG and symmetric S-FG nanobeam using integral Timoshenko beam theory, Adv. Nano Res. 8 (4) (2020) 293–305, https://doi.org/10.12989/anr.2020.8.4.293.
[74] H. Kara, M. Aydogdu, Dynamic response of a functionally graded tube embedded in an elastic medium due to SH-waves, Compos. Struct. 206 (2018) 22–32, https://doi.org/10.1016/j.compstruct.2018.08.032.
[75] J. Chen, X. Zhou, W. Wang, B. Liu, Y. Lv, W. Yang, D. Xu, Y. Liu, A review on fundamental of high entropy alloys with promising high–temperature properties, J. Alloys Compd. 760 (5) (2018) 15–30, https://doi.org/10.1016/j.jallcom.2018.05.067.
[76] H. Chen, X. Yuan, W. Ren, J. Peng, B. Ding, T. Zheng, J. Yu, P. Liaw, Y. Zhong, A new single crystal high entropy alloy with excellent high-temperature tensile property, Mater. Res. Express 7 (4) (2020) 046507, https://doi.org/10.1088/2053-1591/ab8491.